Flow Field Analysis of a Leading-Edge Inflatable Kite Rigid Scale Model Using Stereoscopic Particle Image Velocimetry

Jelle Agatho Wilhelm Poland[1], Erik Fritz[1,2], and Roland Schmehl[1]

[1]Faculty of Aerospace Engineering, Delft University of Technology, Kluyverweg 1, 2629 HS, Delft
[1]TNO, Kessler Park 1, 2288 GS Rijswijk, The Netherlands

Correspondence: Jelle Agatho Wilhelm Poland (j.a.w.poland@tudelft.nl)

Abstract. Leading-edge inflatable (LEI) kites ~~are characterized by a pronounced downward curvature of the wing and flow recirculation zones on the pressure side~~exhibit pronounced anhedral and pressure-side recirculation associated with their double-curved geometry and tubular frame. This study ~~presents novel~~ reports wind tunnel stereoscopic particle image velocimetry (PIV) measurements ~~of~~ around a 1:6.5 ~~rigid scale~~ rigid-scale model of the TU Delft V3 ~~LEI kite. The flow-field measurements were conducted in the Open Jet Facility of Delft University of Technology for two angles of attack and seven chordwise measurement planes positioned~~ kite. Chordwise measurement planes between mid-span and tip ~~, and were compared with results from~~ were acquired at two angles of attack and compared with Reynolds-averaged ~~Navier–Stokes~~ Navier–Stokes (RANS) simulations. ~~The double-curved anhedral wing geometry presented several challenges, such as surface reflections that required careful data processing and the use of a lateral~~ Reflection-prone surface geometry required tailored masking and an additional out-of-plane velocity filter. ~~The circulation distribution was analyzed, using both elliptical and rectangular boundary curves, showing good agreement in trends between the~~ Qualitative comparison confirms that the PIV measurements capture the dominant flow topology predicted by RANS, while revealing local deviations near the surface where measurement limitations become significant. Circulation distributions obtained from contour integration show consistent spanwise trends between vortex-step method (VSM), RANS, and PIV~~data. The~~ , supporting the use of the dataset for model validation. Sectional lift and drag ~~coefficients of each chordwise measurement plane~~ were estimated using the ~~Kutta–Joukowski theorem, surface pressure integration of RANS CFD data~~Kutta–Joukowski relation, RANS surface-pressure integration, and Noca's method—an inherently three-dimensional reformulation of the momentum conservation equations expressed solely as surface integrals over the control-volume boundary~~—applied here~~ , here applied in two dimensions. While ~~the mid-span to tip variation of lift coefficients was in accordance with the anhedral shape~~ sectional lift shows spanwise variation consistent with geometric and tip-vortex ~~effects, the drag measurements and predictions deviated from the expected behavior by exhibiting negative values. Especially near the tip region, significant discrepancies were observed, attributed to increased measurement uncertainty. The surface pressure integration revealed discrepancies at the strut junction, likely due to local~~ influences, drag estimates from near-field PIV exhibit non-physical values, indicating limited robustness of velocity-field-based drag recovery. Local discrepancies near the strut junctions are consistent with three-dimensional strut-induced flow effects ~~and increased airfoil thickness. This study provides comprehensive~~ observed in CFD. The dataset provides validation data for CFD ~~simulations~~ of

LEI kites ~~while highlighting the challenges in PIV measurements of double-curved anhedral wingsand characterizing local aerodynamic phenomena~~and documents practical limitations of PIV applied to strongly curved anhedral wings.

1 Introduction

Leading-edge inflatable (LEI) kites are used for kite-surfing and novel renewable energy applications such as wind-assisted ship propulsion and airborne wind energy (AWE). This specific type of kite uses an inflated tubular frame to collect the aerodynamic load generated by a canopy and transmit this via a system of bridle lines to one or more tethers. Their design as a single morphing aerodynamic control surface makes LEI kites highly ~~maneuverable~~manoeuvrable, which is a crucial requirement for the mentioned applications (Breukels, 2011). Pitch control is achieved by symmetric actuation of the bridle line system (Hummel et al., 2019), directional control by asymmetric actuation (Elfert et al., 2024). The wings are generally downward curved to ~~minimize~~ minimise the spanwise stresses in the bridled membrane structure. While the vertical wing area contributes to the ~~favorable~~ favourable yaw authority, the sweep of the wing extends the depower range of the kite. In addition to the actuation-induced morphing, the shape of the membrane wing is also subject to aero-structural coupling effects. The kite investigated in the present study is illustrated in Fig. 1 and described in more detail ~~in~~ by Oehler and Schmehl (2019).

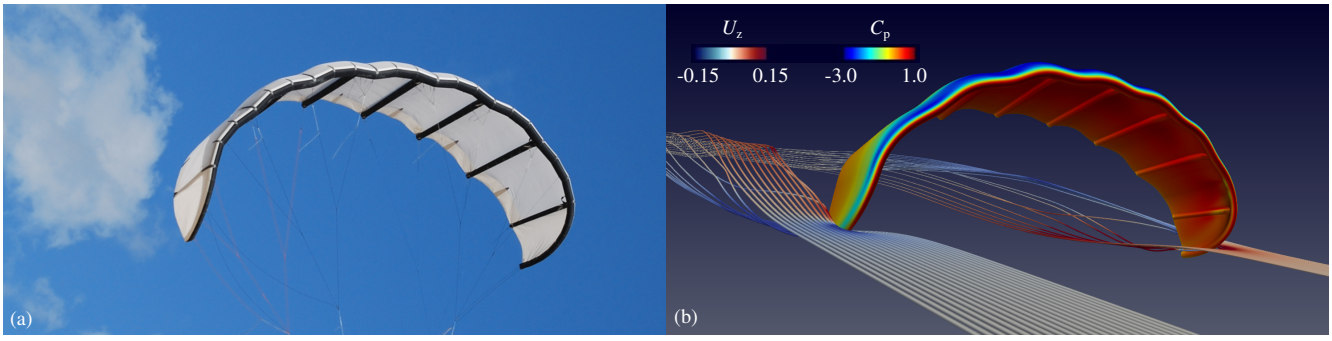

Figure 1. TU Delft V3 kite designed for ~~airborne wind energy~~ AWE harvesting: (a) 2012 prototype with a flat wing surface area of 25 m^2; (b) CFD ~~visualization~~ visualisation of the flow around the design geometry, depicting the non-dimensional surface pressure C_p on the wing and the flow velocity z-component U_z coloring streamlines along the flow around the wing tips (adapted from Viré et al., 2022).

~~Characterizing~~ Characterising the aerodynamics of LEI kites ~~with~~ using numerical prediction and experimental measurement poses ~~several challenges , owing to the highly flexible nature,~~ challenges associated with structural flexibility, pronounced anhedral and sweep, and unconventional airfoil geometries. ~~For example , the backward-facing step formed by the~~ A representative example is the discontinuity at the junction between the inflated leading-edge tube and the attached single-skin canopy~~leads to flow~~ , which promotes pressure-side separation and recirculation ~~zones on the wing's pressure side, already~~ even at low angles of attack. Consequently, fast potential flow solvers can not be used to ~~analyze~~ analyse the two-dimensional (2D) aerodynamics, as was demonstrated in our companion paper (Poland et al., 2025a). Instead, computational fluid dynamics (CFD) solvers based on Reynolds-averaged Navier–Stokes (RANS) equations have to be employed, substantially increas-

ing the computational resource demands for early design iterations (Folkersma et al., 2019). To avoid this computational overhead, which can become excessive when the wing geometry changes continuously, Breukels (2011) derived polynomial approximations of the ~~aerodynamic coefficients C_L, C_D, and C_M~~ sectional aerodynamic coefficients C_l, C_d, and C_m from CFD simulations of a large variety of ~~parametrized~~ parametrised LEI airfoil shapes. ~~Subsequent studies~~ In our companion paper (Poland et al., 2025a), we refined the airfoil ~~parametrization~~ parametrisation and used machine learning to develop regression models with a wider parametric range~~(Watchorn, 2023; Masure, 2025)~~. To expand the 2D aerodynamic properties to three-dimensional (3D) wings, lifting-line methods ~~(Gaunaa et al., 2011; Leloup et al., 2013)~~ (Leloup et al., 2013) and vortex-step methods (VSM) (Damiani et al., 2019; Cayon et al., 2023) have been used successfully. Especially the implementation of ~~pre-computed~~precomputed, shape-dependent airfoil aerodynamic coefficients in the VSM framework ~~proves to deliver~~ delivers high-quality results (Poland et al., 2025a). RANS simulations of complete LEI kites have also been conducted, with parametric sweeps in Reynolds number, angle of attack and sideslip angle, indicating that the strut tubes exert a negligible influence on the integral aerodynamic properties (Viré et al., 2020, 2022).

Experimental analyses of kite aerodynamics are generally most reliable when conducted in a wind tunnel under controlled flow conditions (De Wachter, 2008; Desai et al., 2024). However, industrial-scale kites in the size range of 50 to 500 m^2 can not be mounted at full scale in wind tunnel facilities. On the other hand, reverting to scale models requires preserving aeroelastic similarity, which is challenging for a bridled inflatable membrane structure. A practical option is to decrease the complexity of the fluid-structure interaction problem by investigating the aerodynamics of a rigid scale model, such as presented by Belloc (2015) for a reference paraglider wing. A similar approach was pursued ~~by Poland et al. (2025b), measuring~~ in our companion paper (Poland et al., 2025b), where the aerodynamic loads on a rigid scale model of the TU Delft V3 kite were measured for different angles of attack, sideslip angles, and Reynolds numbers. The measured forces and moments corroborate numerical predictions from CFD and VSM simulations within the nominal operating regime, encompassing angles of attack from 2° to 8° and sideslip angles of ±10°, as reported by Cayon et al. (2025).

Although numerical studies have significantly advanced the understanding of LEI airfoil aerodynamics and integral effects of ~~the~~ airfoil loading, a detailed experimental analysis of the sectional flow around this ~~specific type~~ class of wing has not been reported in the literature. Particle image velocimetry (PIV) offers a non-intrusive method to capture planar flow fields, with minimal influence from introduced tracer particles. Stereoscopic PIV, employing two cameras, mitigates potential errors caused by perspective distortions in velocity measurements (Prasad, 2000). The resulting flow fields enable evaluation of local ~~2D~~ pseudo-2D aerodynamic properties, including circulation, induction, inflow angles, forces, and aerodynamic coefficients (Fritz et al., 2024a). Circulation can be determined by defining a boundary curve and interpolating velocity components along it~~. Forces~~ , and forces may subsequently be estimated on this boundary using Noca's method (Noca et al., 1999).

The present ~~paper describes a novel stereoscopic PIV analysis of a rigid scale model of the TU Delft V3 LEI kite with the goal of obtaining spatially resolved flow-field data. The data was acquired in seven chordwise measurement~~ study addresses this gap by providing stereoscopic PIV measurements in chordwise planes along the ~~wing span , for~~ span of a rigid TU Delft V3 scale model at two angles of attack~~. Sources of uncertainty were systematically assessed, local strut effects were investigated, and a novel masking approach accompanied by a detailed sensitivity analysis was introduced~~, forming the first

geometry-consistent, spatially resolved flow-field dataset for a representative LEI kite configuration. The resulting ~~flow fields were used to calculate local aerodynamic properties, such as circulation and sectional aerodynamic coefficients. The primary outcome is an investigation of underlying aerodynamic phenomena through comparison of experimentally measured and numerically simulated flow fields, conducted qualitatively and quantitatively, the latter based on circulation and 2D force estimates.~~ measurements enable qualitative and quantitative comparison with RANS CFD and VSM predictions, supporting their use in sectional and spanwise load modelling. Although stereoscopic PIV is well established, its application to the strongly anhedral LEI geometry, characterised by extensive pressure-side recirculation, has not been previously documented.

The remainder of the paper is ~~organized~~ organised as follows. Section 2 describes the experimental methodology, including the wind tunnel, rigid scale model, experimental setup, stereoscopic PIV technique, test cases, data processing, and methods for deriving aerodynamic quantities. Section 3 presents the results, including uncertainty analysis, qualitative comparisons between CFD and PIV, and quantitative comparisons. A discussion of the results follows in Sect. 4, addressing PIV measurement limitations, an analysis of quantitative discrepancies, and local strut effects. Conclusions and recommendations for future research are presented in Sect. 5.

2 Method

This section outlines the specifications of the wind tunnel, the scale model, the experimental setup, and the PIV technique. The arrangement of the measurement planes is discussed next, followed by the data processing steps, and a description of how integral aerodynamic quantities are derived from planar flow field data.

2.1 Wind tunnel

The wind tunnel experiments were conducted in the closed-loop Open Jet Facility (OJF) of the TU Delft from 8 to 12 April 2024. The tunnel has an octagonal exhaust nozzle measuring 2.85×2.85 m and is equipped with a 500 kW electric motor and a large fan generating a flow speed up to 35 ms^{-1}. To ensure uniform flow conditions in the test section, the tunnel uses corner guide vanes and wire meshes. The maximum reported turbulence intensity in the test section is 0.5% (Lignarolo et al., 2014). ~~While the load measurements in (Poland et al., 2025b) were done for several wind speeds, the~~ The PIV measurements used a ~~fixed~~ wind speed of $U_\infty = 15$ ms^{-1}, with variations from the set point up to 0.2%. The inflow and atmospheric conditions for each measurement were logged to ~~later be able to correctly non-dimensionalize the data, which~~ enable correct non-dimensionalisation of the data. This was particularly important in this campaign, as the temperature ranged from 22 to 32 °C due to a malfunctioning cooling system. ~~Wind tunnel corrections were needed and applied to the~~

The projected frontal blockage ratio is approximately 3%, for which blockage-induced acceleration and the associated correction to the effective angle of attack ~~to account for blockage effects (Poland et al., 2025b).~~ are expected to be small (Poland et al., 2025b). This assessment is consistent with common wind-tunnel guidance recommending blockage ratios below 7.5% (Barlow et al., 1999). In the OJF, the jet is bounded by turbulent shear layers that originate at the nozzle edges and contract the jet core with a

reported semi-angle of $4.75°$ near the nozzle exit (Lignarolo et al., 2014). With the model centred in the 2.85 m nozzle and a model width of 1.28 m, the wing tips remained approximately 0.8 m from the nozzle edge.

On this basis, open-jet shear-layer effects and blockage corrections are considered negligible for the present dataset. By contrast, streamline-curvature effects measurably modify the effective angle of attack; the corresponding correction values are reported in Table 1, with the underlying analysis documented in the companion paper (Poland et al., 2025b). These corrections are applied to all reported α values.

Table 1. Corrections for angle and drag coefficients (Poland et al., 2025b).

$\Delta\alpha_{\mathrm{i}}\,(^\circ)$	$\Delta\beta_{\mathrm{i}}\,(^\circ)$	$\Delta C_{\mathrm{D}}\,(-)$
$-0.47\,C_{\mathrm{L}}$	$-0.46\,C_{\mathrm{S}}$	$-0.0078\,C_{\mathrm{L}}^2 - 0.0078\,C_{\mathrm{S}}^2$

2.2 Rigid scale kite model

A rigid wing was used to decouple aerodynamics from aeroelasticity, enabling geometry-consistent, well-controlled measurements that provide unambiguous validation data for numerical models. Such a one-to-one comparison is not feasible for a scaled, flexible AWE-sized kite wing because aeroelastic similarity cannot be preserved: simultaneous matching of Reynolds number, mass distribution, structural stiffness, membrane pretension, and damping is not achievable in a practical wind-tunnel setup. The rigid configuration isolates the aerodynamic response of a well-defined reference geometry, so that discrepancies between measurements and simulations can be attributed primarily to aerodynamic modelling assumptions rather than to uncertain, unmeasured deformation states.

To manufacture a rigid scale model of the V3 kite, the wing geometry adapted for the CFD simulations by Viré et al. (2022) was used, as detailed in the companion paper (Poland et al., 2025b). This CFD geometry differed slightly from the original design: the bridle line system was omitted, the trailing edge connecting the upper and lower wing surfaces was rounded, and edge fillets were applied to all tubular frame–to–canopy connections. Using the CFD geometry was motivated by the measurement data's intended purpose for validating computational studies. The wing was scaled down by a factor of 1:6.5, resulting in the dimensions outlined in Table 2, and the Reynolds number

$$\mathrm{ReRe} = \frac{\rho U_\infty c_{\mathrm{ref}}}{\mu} = 3.8 \times 10^5, \tag{1}$$

where $\rho = 1.2$ kgm^{-3} denotes the density, $U_\infty = 15$ ms^{-1} the inflow speed, $c_{\mathrm{ref}} = 0.396$ m the reference chord, and $\mu = 1.89 \times 10^{-5}$ the dynamic viscosity. The scale model mounted in the test section is shown in Fig. 2. (a), with a rear view of the wing tip in (b). The image highlights the smooth transition between the circular leading-edge tube and the membrane surface. Although the idealised CFD geometry also incorporates fillets in this region, the manufactured scale model exhibits slightly larger radii due to manufacturing constraints.

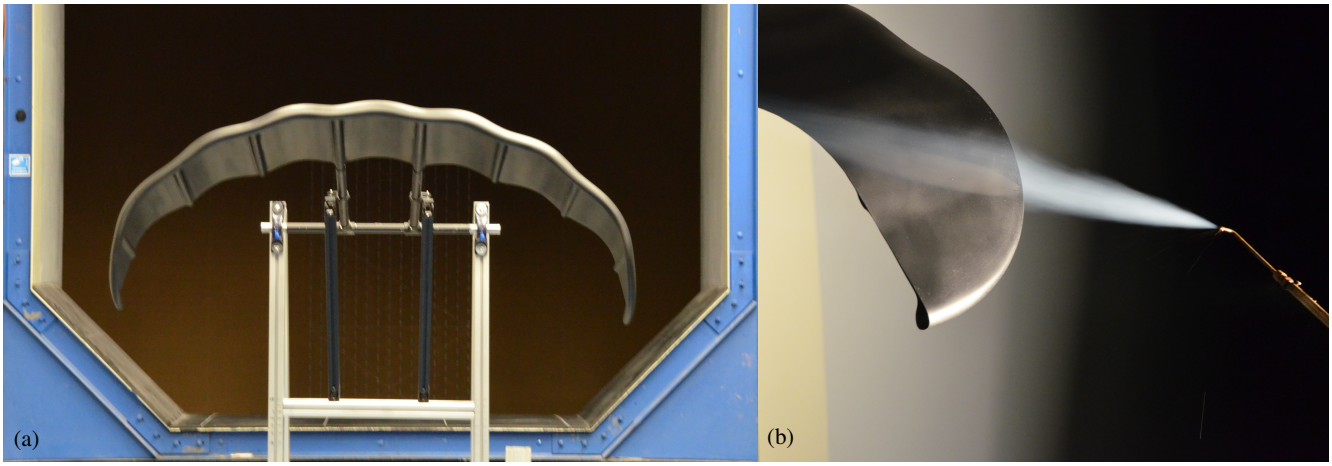

Figure 2. Wind tunnel setup: (a) Rigid scale model in the wind tunnel, ~~swiveled~~ swivelled by ~~180 °~~ 180° with its back facing the octagonal OJF exhaust nozzle; (b) ~~Smoke~~ Rear view showing a smoke trail visualisation of the flow over a wing tip, and indicating the fillet between the circular leading edge and the canopy.

Table 2. Dimensions of the 1:6.5 scale model. Chord length, height, and width of the manufactured model deviate by no more than 1 mm from the scaled geometry, as verified using a laser tracker (Poland et al., 2025b).

Property	Symbol	Value	Unit
Mid-span chord	c_{ref}	0.396	m
Height	h	0.462	m
Width	W	1.278	m
Mass	m	7.965	kg
Flat surface area	S	0.59	m^2
Planform area	A	0.46	m^2
Projected frontal area at $\alpha = 24°$	A_{f}	0.2	m^2

2.3 Experimental setup

The scale model is positioned in the ~~center~~ centre of the octagonal jet-exhaust using a support structure of ~~aluminum~~ aluminium beams. Two steel rods extend from the wing's ~~center~~ centre struts and connect the scale model to the support frame, as shown in Fig. 2(a) and detailed in the companion paper (Poland et al., 2025b). The images in Fig. 3 depict the normal and upside-down configurations, respectively, for ~~analyzing~~ analysing the flow field on both sides of the wing with the cameras positioned on the ground. The highlighted horizontal bar was used to adjust the angle of attack α of the wing, achieving an accuracy of $0.1°$ as measured by digital inclinometers. Both the cameras and the laser were mounted on a ~~motorized~~ motorised traverse system with a step size of 0.01 mm in the x and y directions. This configuration permitted measurements at multiple chordwise (x) and transverse (y) locations without the need to refocus the cameras or recalibrate the software. Due to the wing's downward

curvature, the distance between the PIV system and the measurement plane varied. To ensure the wing remained within the camera field of view, its vertical position was adjusted for certain measurements by raising the blue table supporting the structure, as shown in Fig. 3.

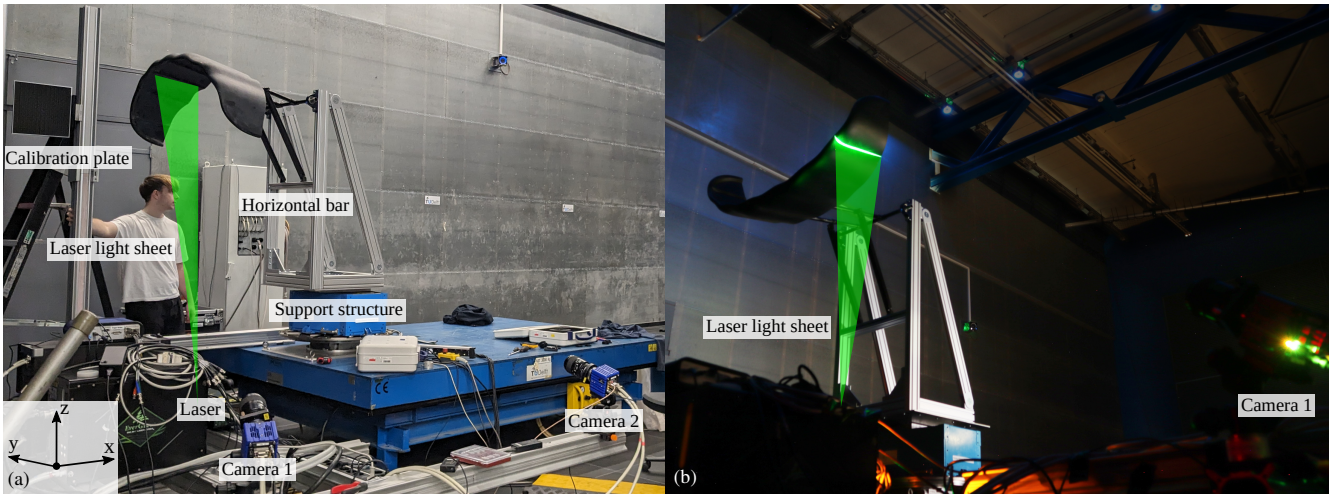

Figure 3. Experimental setup: (a) Photograph showing the labelled components of the setup and the axis orientations; (b) Long-exposure photo of the laser light sheet projected onto the model. In this instance, the laser light sheet spans the entire chord, a coverage not typical during standard measurements, achieved here by operating the system in laser alignment mode. In both photos, the laser light sheet was graphically enhanced.

2.4 Stereoscopic particle image velocimetry

The flow field around the wing was measured non-intrusively with stereoscopic ~~particle image velocimetry (PIV)~~PIV. The flow, seeded with tracer particles, was captured by two synchronised cameras, each recording pairs of images with a time delay of 100 µs. The flow field was determined by comparing these sets and tracking the displacement of particle groups. Laser control, camera ~~synchronization~~synchronisation, and image acquisition were all triggered by a single pulse signal from an opto-coupler (TCST 2103), controlled via LaVision's DaVis 8 software. For each plane, each camera recorded a total of 250 image sets at 15 Hz, which, as demonstrated in Fig. A1 in ~~Appendix~~App. A, was sufficient to ensure statistical convergence for time-averaged results.

A Quantel Evergreen double-pulsed neodymium-doped yttrium ~~aluminum~~ aluminium garnet laser was used as the light source, with a wavelength λ_L of 532 nm, shaped into an approximately 3 mm thick laser light sheet. As illustrated in Fig. 3, the generated vertical sheet illuminates a flow-aligned cross-section of the floor-facing side of the wing. To reduce light reflections, both the wing and relevant parts of the support structure were spray-painted matte black. A Safex smoke generator produced tracer particles with a median diameter of 1 µm. The generator was positioned downstream of the tunnel test section to ensure a homogeneous mixing of the particles with the flow before re-entering the test section.

The two LaVision Imager sCMOS cameras, with an f-number $f_\# = 8$, defined as the ratio between focal length and aperture diameter (Raffel et al., 2018), were placed at radial distances of 1.70 and 1.95 m from the laser light sheet. This configuration resulted in a field of view (FOV) of 0.42×0.36 m. The cameras had a sensor resolution of 2560×2160, a pixel size $p_{\text{size}} = 6.5$ µm corresponding to a spatial sampling density of 6.41 pixels per ~~millimeter~~millimetre. The magnification factor M, defined as the image size divided by the object size, was computed along the x-axis. A sensor width of 2160 px with a pixel size of 6.5 µm, over a 0.36 m-wide field of view, resulted in a value of $M = 0.039$. The ratio of the diffraction diameter of the particles to the pixel diameter is recommended to be higher than one to ~~minimize~~ minimise peak locking errors (Raffel et al., 2018; Bensason et al., 2025). It was calculated using

$$\frac{d_{\text{diff}}}{p_{\text{size}}} = \frac{2.44 f_\# (M+1)\lambda_L}{p_{\text{size}}} = 1.7. \tag{2}$$

The cameras were calibrated using a target with a known grid pattern, visible as a black square on the left side of Fig. 3(a). The calibration was verified by comparing the measured distances between reference points with their known physical spacing.

2.5 Test cases

Because the scale model is symmetric with respect to the ~~center~~ centre chord and only symmetric inflow conditions were considered, the measurements were limited to one half of the wing. Seven measurement planes denoted as $Y1$ through $Y7$ were selected, as shown in Fig. 4. To align with available CFD simulation results, the measurements were conducted at angles of attack ~~$\alpha = 7$~~ $\alpha = 7°$ and 17°, with the larger value also covering stall phenomena (Poland et al., 2025a).

The positions of the bottom left corners of the measurement planes for the suction-side-up configuration, shown in Fig. 5, are listed in Table 3 and measured relative to the mid-span leading-edge point. The table height was kept fixed for $Y1$ through $Y4$, and ideally, the vertical position z at the top of each measurement plane would be zero. However, small offsets were observed and attributed to minor imperfections in the experimental setup. These offsets were corrected in the post-processing by aligning the raw image light intensity with the expected cross-section location. For each measurement plane, the images were iteratively shifted until a precise match was achieved.

As visible in Fig. 4, only the mid-span plane $Y1$ was perpendicular to the wing surface. Moving outwards from $Y1$ to $Y7$, the vertical planes became progressively more aligned with the wing surface as a result of its downward curvature. Toward the tip, this alignment caused the velocity component normal to the measurement plane to increase, which is more difficult to accurately capture (Prasad and Adrian, 1993; Prasad, 2000). ~~Due to time constraints, the measurements at $\alpha = 17$ ° were limited to~~ At $\alpha = 17$ °, measurements were obtained for planes $Y1$ ~~through~~ $Y4$, but only planes meeting the data-quality and uncertainty criteria were retained for analysis.

2.6 Data processing

The measurements were processed using LaVision's DaVis 10 software (LaVision GmbH, 2025). The procedure consisted of the following steps: (1) averaging the image sequence; (2) ~~normalizing~~ normalising each image by the computed average; (3) applying a temporal filter with a filter length of five images; (4) applying masks to exclude regions not of interest; (5)

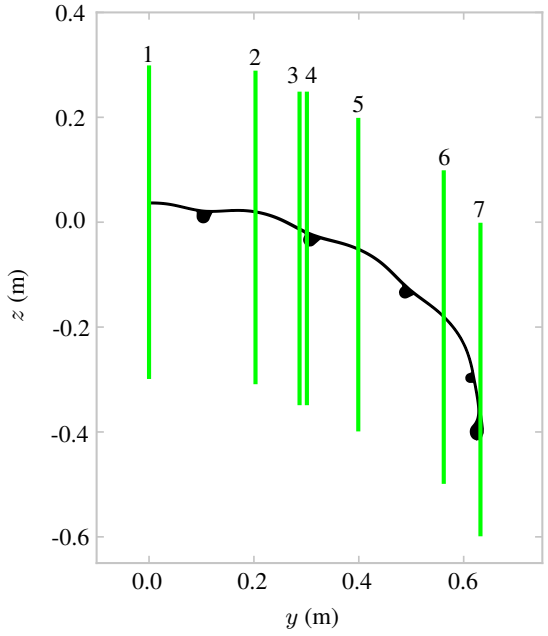

(a)

Figure 4. Arrangement of the measurement planes along the span, for $\alpha = 7^\circ$ at 10% x/c aft of the mid-span leading edge.

Table 3. ~~Reference positions~~ Bottom left corners of the measurement planes, ~~i.e., bottom left corners, see~~ shown in Fig. 5, at $\alpha = 0^\circ$.

	x (m)	y (m)	$z_{\alpha=7}$ (m)	$z_{\alpha=17}$ (m)
$Y1$	0	0.000	-0.000	-0.000
$Y2$	0	0.203	-0.004	-0.000
$Y3$	0	0.287	-0.001	-0.001
$Y4$	0	0.301	-0.005	-0.006
$Y5$	0	0.399	-0.120	—
$Y6$	0	0.562	-0.111	—
$Y7$	0	0.632	-0.244	—

performing the PIV analysis using interrogation windows of 64×64 px^2 with two passes and 50% overlap; and (6) averaging the resulting vectors, including only data with at least 25 source vectors and falling within two standard deviations of the mean. The first and second steps ~~normalize~~ normalise the local light intensity to enhance particle detection, which proved particularly useful in regions affected by reflections.

~~For each y location, six overlapping measurements were taken, as shown~~ For each measurement plane, six partially overlapping sub-planes were acquired and combined into a single field on a common grid, illustrated in Fig. 5. ~~The data in the overlapping regions were stitched together to form a continuous flow field. The grid was evaluated sequentially along rows, corresponding to the x-direction. To ensure a smooth transition, data points from overlapping measurements were weighted based on their relative distance from the edges of the combined region.~~ Each sub-plane was first shifted to a shared coordinate system and interpolated onto the common grid. Non-overlapping regions were copied directly. In overlap regions, values from the two contributing sub-planes were blended using a smooth sigmoid ramp to avoid discontinuities. Across an overlap of length L, a normalised coordinate $x \in [0,1]$ was defined and the weight

$$w(x) = \frac{1}{1 + \exp\left[-10\left(x - \frac{1}{2}\right)\right]} \tag{3}$$

was applied, such that the stitched value is $(1-w)\,\phi_1 + w\,\phi_2$, where ϕ_1 and ϕ_2 denote the fields from the two sub-planes. A steepness parameter of ten was chosen empirically to balance smoothness and transition width. The same blending procedure was used for both streamwise and transverse stitching and was applied identically to all reported variables. In the remainder of the paper, the result of stitching these six measurements is referred to as a single measurement plane.

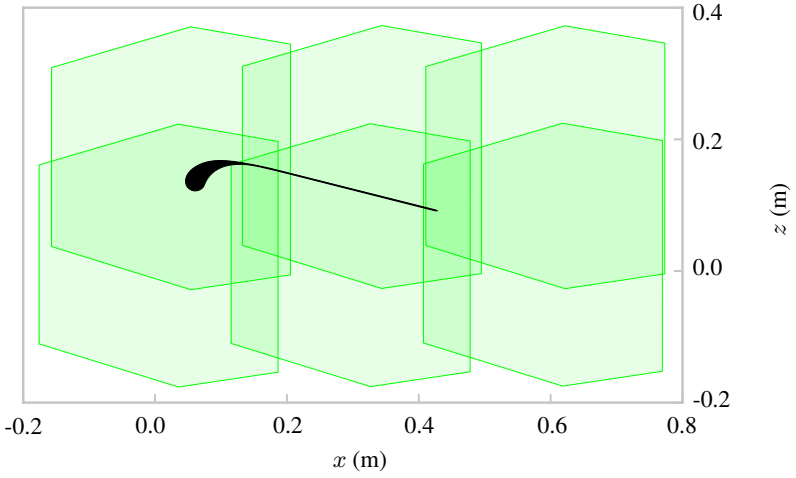

(a)

Figure 5. Mid-span cross-sectional view showing the LEI airfoil and the six overlapping measurement regions that together form plane $Y1$. The intentional overlap ensures full coverage of the flow field.

2.7 Derivation of integral aerodynamic quantities

The PIV measurements yield ~~2D~~ datasets of scalar- and vector-valued flow field properties, including the spatial coordinates $\mathbf{x}$, the streamwise, lateral, and vertical components u_x, u_y, and u_z, respectively, the velocity magnitude u, and the spatial derivatives of the velocity components. From this discrete data, the components u_x and u_z are interpolated along a suitable closed planar boundary curve S around the airfoil. In the present study, this boundary is defined as a closed planar curve within a single measurement plane, such that the resulting force estimates represent sectional, pseudo-2D loads per unit span and neglect out-of-plane momentum transport. This allows for the computation of the circulation Γ as a line integral of the velocity field

$$\Gamma = \oint_S \mathbf{u} \cdot \mathrm{d}\mathbf{s}, \tag{4}$$

quantifying the rotational strength of the flow in that region. Given the circulation, the 2D lift per unit span can be approximated using the Kutta–Joukowski theorem (Anderson, 2016)

$$C_{\text{l',Kutta}} = \frac{2\Gamma}{U_\infty c_{\text{ref}}}. \tag{5}$$

This equation assumes that the integration boundary lies within the potential flow region surrounding the object of interest and that the flow is steady and attached. Nevertheless, although derived from an inviscid formulation, the circulation-based method retains theoretical validity in viscous flows, with Liu et al. (2015) proving the exact applicability of the Kutta–Joukowski relation under steady 2D viscous and compressible conditions. ~~In the present context, these assumptions are only approximately satisfied, as the flow is incompressible and quasi-steady but~~ Because the flow is locally 3D and ~~measured in the near field, so that circulation-based estimates should be interpreted as approximate rather than exact~~Γ is evaluated from a single measurement plane, out-of-plane transport is not captured; the resulting value is therefore interpreted as an approximate sectional lift coefficient based on U_∞ and c_{ref}.

~~An alternative approach for force estimation is based on integrating the momentum change over a finite control volume . However, when using PIV measurements , reflections from the object surface often prevent reliable data acquisition near the body.~~ The aerodynamic force on an airfoil can be obtained from the integral momentum balance over a fixed control volume V bounded by a closed surface S with outward unit normal $\mathbf{n}$. For an incompressible, statistically steady flow,

$$\mathbf{F}_{\mathrm{body}} = \int_S (-p\,\mathbf{n} + \boldsymbol{\tau}\cdot\mathbf{n})\,\mathrm{d}S - \int_S \rho\,\mathbf{u}\,(\mathbf{u}\cdot\mathbf{n})\,\mathrm{d}S, \tag{6}$$

where $\mathbf{F}_{\mathrm{body}}$ denotes the net aerodynamic force on the body, p the static pressure, $\mathbf{u}$ the velocity field, and $\boldsymbol{\tau}$ the viscous stress tensor. In special cases, pressure contributions can be minimised by choosing a control surface that extends sufficiently far into the wake such that static pressure has recovered to p_∞ and viscous traction on the outer boundary is negligible. Under these conditions, drag may be estimated from the far-wake streamwise momentum deficit, whereas lift follows from the transverse momentum balance associated with wake downwash and vorticity. In both cases, the pressure-free simplification requires a far-field control surface that encloses the full wake and lies in a region of pressure recovery. For lift in particular, accurate force recovery additionally requires that the control surface captures the spatial extent of the induced velocity field, since truncation of the lateral or vertical boundaries introduces non-negligible momentum and pressure-flux contributions associated with downwash and tip-vortex transport.

These conditions are not satisfied for the present dataset. The available PIV measurements are confined to the near field, so that any admissible control surface would necessarily intersect regions of separated flow, shear layers, and the developing wake, where static pressure has not recovered to p_∞ and contributes non-negligibly to the surface integral momentum balance. Consequently, neither drag nor lift can be obtained from a pressure-free control-volume formulation without an additional pressure-reconstruction step, which is not accessible from planar PIV data alone.

Moreover, as discussed in Sect. 3, near-wall velocity data are incomplete, preventing direct evaluation of the momentum flux through a closed control surface surrounding the body. Any attempt to apply the classical control-volume balance would therefore require substantial modelling assumptions to reconstruct both the pressure distribution and the masked near-wall velocity field, rendering the approach ill-posed under the present experimental constraints.

Noca et al. (1999) proposed an alternative formulation of the momentum conservation equations that ~~relies solely on surface integrals of flow quantities evaluated along the boundary of the control volume. This approach facilitates force estimation from~~

flow field measurements without requiring velocity data throughout the entire control volume. Noca'expresses aerodynamic forces in terms of boundary integrals involving velocity, vorticity, and their temporal and spatial derivatives. Although Noca's method involves higher-order velocity gradients and temporal derivatives that are sensitive to measurement noise, it enables a closed force formulation under the present experimental constraints. Noca's method has been successfully applied in such contexts to flow data from both similar PIV-based force estimation studies, including horizontal-axis wind turbines(Fritz et al., 2024a, b) (Fritz et al., 2024a, b) and vertical-axis wind turbines(LeBlanc and Ferreira, 2022). (LeBlanc and Ferreira, 2022). The method, expressed in symbolic notation, evaluates the force per unit density as,

$$\frac{\mathbf{F}}{\rho} = \oint_{S} \mathbf{n}\cdot\boldsymbol{\gamma}_{\text{flux}}\,\mathrm{d}s - \oint_{S_\text{b}} \mathbf{n}\cdot(\mathbf{u}-\mathbf{u}_\text{b})\,\mathbf{u}\,\mathrm{d}s - \frac{d}{dt}\oint_{S_\text{b}} \mathbf{n}\cdot(\mathbf{u}\mathbf{x})\,\mathrm{d}s, \tag{7}$$

where

$$\begin{aligned}\boldsymbol{\gamma}_{\text{flux}} =& \frac{1}{2}u^2\mathbf{I} - \mathbf{u}\mathbf{u} - \frac{1}{\mathscr{N}-1}\mathbf{u}(\mathbf{x}\times\boldsymbol{\omega}) + \frac{1}{\mathscr{N}-1}\boldsymbol{\omega}(\mathbf{x}\times\mathbf{u})\\ &- \frac{1}{\mathscr{N}-1}\left(\mathbf{x}\cdot\frac{\partial\mathbf{u}}{\partial t}\right)\mathbf{I} + \frac{1}{\mathscr{N}-1}\mathbf{x}\frac{\partial\mathbf{u}}{\partial t} - \frac{\partial\mathbf{u}}{\partial t}\mathbf{x}\\ &+ \frac{1}{\mathscr{N}-1}[\mathbf{x}\cdot(\boldsymbol{\nabla}\cdot\boldsymbol{\tau})]\,\mathbf{I} - \frac{1}{\mathscr{N}-1}\mathbf{x}(\boldsymbol{\nabla}\cdot\boldsymbol{\tau}) + \boldsymbol{\tau},\end{aligned} \tag{8}$$

and $\mathbf{n}$ is the normal vector on the bounding curve, S is the outer boundary curve of the control volume surrounding the immersed body, S_b is the inner boundary curve prescribed by the immersed body's surface, $\mathbf{u}_\text{b}$ is the velocity vector of the immersed body's surface, $\mathscr{N}$ represents the number of dimensions, ~~$\boldsymbol{\omega}$ the angular velocity vector of the immersed body~~$\boldsymbol{\omega} = \boldsymbol{\nabla}\times\mathbf{u}$ is the flow vorticity, $\mathbf{x}$ is the position vector, $\mathbf{I}$ the identity tensor, and $\boldsymbol{\tau}$ the viscous stress tensor. In the present pseudo-2D application, S and S_b are closed planar curves and $\mathrm{d}s$ denotes arc length.

The second term on the right-hand side of Eq. (7) represents the advective momentum flux through the body ~~surface. Because the scale model has a solid,~~ boundary. For an impermeable surface, ~~this contribution vanishes.~~ the no-throughflow condition enforces $\mathbf{n}\cdot(\mathbf{u}-\mathbf{u}_\text{b}) = 0$ on S_b, hence this term vanishes. The third term ~~is also zero, as it accounts for forces due to boundary acceleration. In the present case, the scale model is assumed to remain stationary , and, because~~ also vanishes for the present stationary model ($\mathbf{u}_\text{b} = \mathbf{0}$), because on S_b the no-throughflow condition ~~on the body surface,~~ implies $\mathbf{n}\cdot\mathbf{u} = 0$ ~~, also enforces the product $\mathbf{n}\cdot(\mathbf{u}\mathbf{x})$ to vanish~~and therefore $\mathbf{n}\cdot(\mathbf{u}\mathbf{x}) = (\mathbf{n}\cdot\mathbf{u})\,\mathbf{x} = \mathbf{0}$.

Equation (8) describes ten individual contributions: the first four, presented in the first line, are inviscid contributions~~,~~; the following three ~~are time-dependent and are zero for steady flow. The final three contributions~~ represent unsteady terms associated with local acceleration; and the final three account for viscous effects. ~~While Noca'~~Because the present force estimates are evaluated from time-averaged, statistically steady velocity fields, the explicit time-derivative contributions in Eq. (8) vanish in the formulation adopted here. While Noca's method is inherently 3D, it ~~is~~ was here applied to a ~~pseudo 2D~~ pseudo-2D incompressible flow problem by setting the out-of-plane velocity u_y to zero. Other out-of-plane quantities, such as the vorticity component ω_y, ~~are~~ were retained, consistent with the ~~pseudo 2D~~ pseudo-2D flow assumption. This simplification ~~reduces the expression accordingly, see App. B for~~ reduced the governing equations accordingly; the full derivation ~~. The~~

~~resulting 2D method facilitates the calculation of normal and tangential force components from a defined boundary path in a flow field.~~ is provided in App. B.

Since the CFD simulations provide the flow field for the entire domain, 2D aerodynamic forces can also be derived ~~via~~ from surface pressure and ~~surface shear force integration~~shear force integrations. Here, the integration was performed over sectional airfoil surfaces, yielding pseudo-2D aerodynamic loads directly comparable to planar PIV-based force estimates. The total aerodynamic force acting on the airfoil section is computed as

$$\mathbf{F} = \underline{\rho} \oint_{S_\mathrm{b}} \underline{\mathbf{n}\cdot}\,(-p\mathbf{I} + \boldsymbol{\tau})\, ~~\mathrm{d}\cdot\mathbf{n}~~\,\mathrm{d}s, \tag{9}$$

where p ~~represents~~ is the static pressure and $\boldsymbol{\tau}$ is the viscous stress tensor.

3 Results

This section presents the results obtained from stereoscopic PIV experiments, including an uncertainty assessment, a qualitative comparison of measured and simulated velocity fields, and a quantitative analysis of circulation and aerodynamic loads. ~~Masking procedures were necessary due to surface reflections.The~~

3.1 Uncertainty analysis

Following PIV uncertainty practice, we distinguish Type-A (statistical) from Type-B (systematic/modelling) contributions (Sciacchitano and . The values in Table 5 quantify the Type-A uncertainty of the estimated mean velocity due to the finite ensemble size. Systematic contributions (Type-B) such as stereo-calibration/mapping residuals, correlation bias (peak locking), finite light-sheet thickness, masking/interpolation, stitching, and measurement-plane misalignment are discussed separately.

Among the systematic (i.e., non-random, repeatable) effects, two experiment-specific effects dominated the present dataset. First, reflection-induced artefacts near the surface necessitated an additional out-of-plane velocity mask using the criterion $|u_y| > 3\ \mathrm{ms}^{-1}$; this threshold was applied as a diagnostic filter to suppress stereo-reconstruction failures in reflection-prone regions rather than as a physical constraint on genuine 3D flow (App. C). Second, increasing measurement-plane misalignment towards the wing tip amplified out-of-plane transport and progressively reduced the validity of pseudo-2D sectional balances, thereby compromising near-wall data and the applicability of sectional momentum-based analyses.

To quantify the resulting information loss, Table 4 reports a plane-wise breakdown of vectors removed by successive quality-control steps. The fraction f_{nan} denotes vectors rejected by correlation and validation procedures and primarily reflects reflection- and geometry-driven loss of correlation, including specular reflections, laser shadowing, regions outside the illuminated laser sheet, and locally insufficient seeding. From the remaining valid vectors, f_{u_y} denotes the fraction removed by an additional out-of-plane velocity filter, $|u_y| > 3\ \mathrm{ms}^{-1}$, applied in post-processing to suppress stereo-reconstruction failures in reflection-prone regions; further details are provided in App. ~~??~~C.

3.2 ~~Uncertainty analysis~~

Table 4. Breakdown of data-quality fractions per measurement plane. f_{nan} denotes the fraction of vectors flagged invalid, f_{u_y} the fraction removed by the out-of-plane velocity filter ($|u_y| > 3\,\mathrm{m\,s^{-1}}$, see App. C), and f_{valid} the remaining valid fraction.

	$\alpha = 7°$							$\alpha = 17°$			
	$Y1$	$Y2$	$Y3$	$Y4$	$Y5$	$Y6$	$Y7$	$Y1$	$Y2$	$Y3$	$Y4$
f_{nan} (%)	51.6	50.3	50.4	50.8	48.8	54.9	52.3	53.4	55.8	56.3	58.7
f_{u_y} (%)	5.7	6.5	8.9	8.9	12.9	7.5	9.6	5.6	9.4	10.7	10.2
f_{valid} (%)	42.7	43.2	40.7	40.3	38.3	37.6	38.1	41.0	34.8	32.9	31.2

~~The uncertainty in velocity measurements for~~

The results in Table 4 show that the dominant reduction in usable data originates from f_{nan}, which accounts for approximately half of the field across all planes. This arises, in large part, from obstruction of the cross-section and, in some planes, the support structure, as shown in Fig. 6. The out-of-plane velocity filter contributes an additional 6–13% loss, with the loss increasing towards the wing tip, where 3D effects and measurement-plane misalignment become more pronounced.

Despite these data quality reductions, the sample size was sufficient to ensure convergence of the time-averaged ~~analyses can be expressed using the standard uncertainty $u_{\bar{u}}$ (Sciacchitano and Wieneke, 2016; Huang et al., 2023; Bensason et al., 2025),~~ velocity statistics, as demonstrated in App. A. Following common PIV uncertainty practice, the Type-A (precision) uncertainty of the mean velocity is quantified from the sample standard deviation of the measured velocity time series and the number of samples (Sciacchitano and Wieneke, 2016). For a two-sided 95% confidence interval, the expanded Type-A uncertainty of the mean is written as

$$u_{\bar{u}} = k \frac{\sigma_u}{\sqrt{N}}, \tag{10}$$

where σ_u is the sample standard deviation, N is the number of ~~images, and $k = 1.96$ denotes~~ image pairs, and k is the coverage factor~~corresponding to a 95% confidence interval. Average velocity uncertainties are summarized in~~. For the present dataset ($N = 250$), using the normal-approximation coverage factor $k = 1.96$ instead of the exact Student-t value changes $u_{\bar{u}}$ by less than 0.5%. Temporal correlation between successive image pairs is not explicitly accounted for; if present, it reduces the effective sample size and may therefore moderately underestimate the Type-A uncertainty.

Table 5 ~~. The data indicate that uncertainties increase toward the wingtip, which is consistent with greater~~ summarises $u_{\bar{u}}$ for each velocity component, obtained by evaluating the sample standard deviation over the $N = 250$ image pairs at each grid point and aggregating the result per measurement plane. The uncertainty levels increase towards the wing tip, consistent with increasing measurement-plane misalignment and enhanced surface reflections. At ~~an angle of attack of~~ $\alpha = 17°$, where stall was anticipated from integral load measurements (Poland et al., 2025b), uncertainties are significantly higher~~. These observed~~, consistent with increased flow unsteadiness and intermittency in separated regions and stitching errors. These trends should be taken into account when interpreting the subsequent qualitative and quantitative analyses. Compared to the mean inflow velocity, the reported uncertainties correspond to approximately 0.2%–0.7% at $\alpha = 7°$, increasing to about 0.7%–1.7% at $\alpha = 17°$.

Table 5. ~~Velocity standard~~ Expanded uncertainties ~~,~~ of the mean velocity corresponding to a ~~95%~~ 95% confidence interval ($k \approx 1.96$), ~~were~~ calculated ~~based on 250 images~~ from $N = 250$ samples and aggregated over all data points within a ~~single~~ measurement plane. These values quantify statistical convergence only and do not include systematic (Type-B) contributions.

	$\alpha = 7°$							$\alpha = 17°$			
	$Y1$	$Y2$	$Y3$	$Y4$	$Y5$	$Y6$	$Y7$	$Y1$	$Y2$	$Y3$	$Y4$
$u_{\bar{u},x}$ (ms^{-1})	0.03	0.04	0.04	0.04	0.04	0.05	0.05	0.11	0.12	0.11	0.13
$u_{\bar{u},y}$ (ms^{-1})	0.06	0.07	0.07	0.07	0.08	0.07	0.08	0.14	0.19	0.19	0.22
$u_{\bar{u},z}$ (ms^{-1})	0.06	0.07	0.07	0.07	0.09	0.08	0.09	0.13	0.21	0.21	0.25
$u_{\bar{u}}$ (ms^{-1})	0.07	0.08	0.08	0.08	0.09	0.09	0.10	0.18	0.23	0.22	0.26

In addition to the statistical (Type-A) uncertainty quantified in Table 5, a systematic contribution arises from the stitching of partially overlapping PIV sub-planes. The magnitude of residual velocity differences across overlap regions is quantified independently in App. D and provides a location-specific indicator of stitching-related variability that is not captured by the statistical uncertainty of the mean.

3.2 Qualitative comparison

The measured velocity fields are compared qualitatively against corresponding slices from CFD simulations by Viré et al. (2022), extracted at the same locations. The CFD results presented here have been corrected for a $1.02°$ offset in angle of attack, defined as the angle between the mid-span chord line and the apparent wind vector (Poland et al., 2025b). This constant offset accounts for a difference in α definition and zero reference between the CFD and the experiment, whereas the streamline-curvature correction in Table 1 is applied to the experimental angles to account for wind-tunnel interference effects. Velocity magnitude fields for the measurement planes are shown in Fig. 6 for sections $Y1$, $Y3$, and $Y4$ at $\alpha = 7°$, and for $Y1$ at $\alpha = 17°$. This specific subset was selected for the qualitative comparison, as these planes report the lowest stitching uncertainty (App. D).

CFD results, available only at a ~~$Re = 10 \times 10^5$~~ $Re = 10 \times 10^5$, are compared against measurements conducted at 3.8×10^5 under the assumption that Reynolds number differences are negligible. This assumption is supported by previous analysis of integral 3D forces and moments, which demonstrated convergence for increasing ~~Re~~ Re from 1.3×10^5 to 5×10^5 using the same experimental setup, model, and wind tunnel (Poland et al., 2025b).

When examining the pressure side, notable discrepancies between the CFD and PIV velocity fields are observed. Both datasets capture the anticipated separation zone downstream of the leading-edge tube; however, the PIV measurements indicate a comparatively larger region of reduced velocity, shown as dark blue areas adjacent to the airfoil surface in Fig. 6. These lower-velocity regions occasionally extend several chord lengths from the airfoil, an effect absent in the numerical predictions. A similar discrepancy is observed on the suction side, particularly at measurement planes $Y3$ and $Y4$ for $\alpha = 7°$, where the PIV data exhibit reduced velocity magnitudes in regions where the simulations predict peak velocities associated with the suction-side low-pressure region. These anomalous low-velocity regions in the PIV ~~data, inconsistent with~~ fields, which are

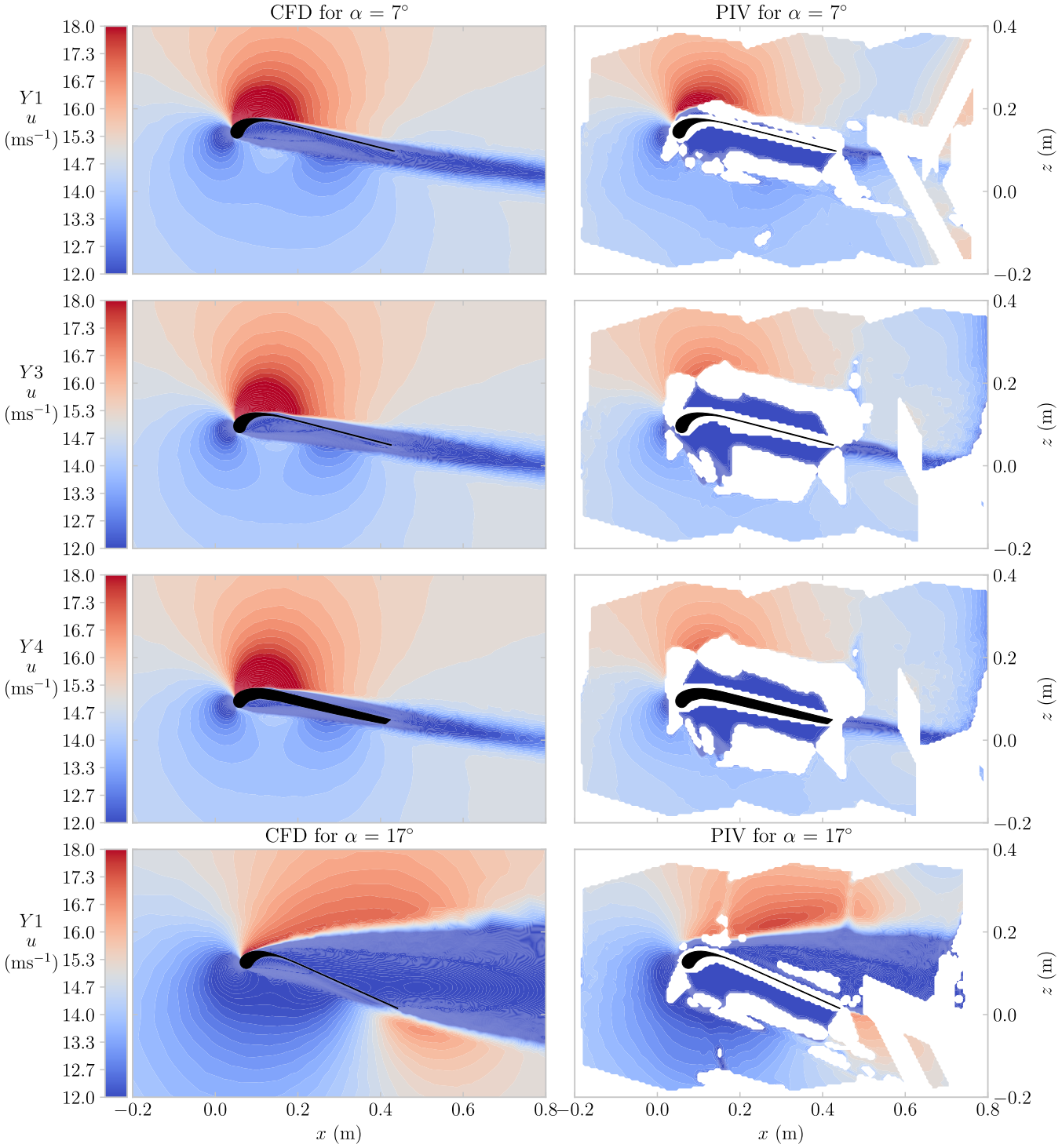

Figure 6. ~~Comparing~~ Comparison of CFD-predicted ~~to~~ and PIV-measured ~~flow~~ velocity-magnitude fields u. The first column shows ~~the computed velocity magnitude u~~ CFD slices extracted at the ~~exact~~ measurement-plane locations, ~~as~~ and the ~~PIV measured results are shown in the~~ second column ~~. The rows in order are~~ shows the corresponding PIV results~~of~~ . Rows (top to bottom) show planes $Y1$, $Y3$, and $Y4$ ~~with α is 7°~~ at $\alpha = 7°$, and plane $Y1$ ~~with α is 17°~~ at $\alpha = 17°$.

inconsistent with the CFD results and with aerodynamic expectations, are ~~attributed primarily to~~ considered to be dominated by persistent surface reflections that were not fully mitigated by the u_y-component masking approach. Although these unresolved regions complicate the qualitative comparison, their impact on the quantitative analysis is minimal, as the selected integration boundary curves typically avoid intersecting such problematic areas.

Away from the airfoil surface, the qualitative comparison improves significantly, with both PIV and CFD velocity fields showing consistent magnitudes, e.g., in the wake region downstream of the wing. At $\alpha = 17°$, both the measurements and simulations consistently capture key flow features, including suction-side flow separation, a reduced velocity increase on the suction side, shear layer development, and the associated velocity gradients across this layer—indicating overall agreement in regions minimally affected by surface reflections. The suction-side flow regions confirm the anticipated stall regions from analysis of the 3D integral forces (Poland et al., 2025a).

3.3 Quantitative results

Aerodynamic properties were computed by integrating ~~flow field data along parameterized~~ the flow field along parameterised boundary curves. Two curve geometries—elliptical and rectangular—were ~~assessed~~considered, as illustrated in Fig. 7. Each ~~boundary~~ curve is defined by ~~a center~~ its centre position, rotation angle, width, height, and ~~a specified~~ number of boundary nodes. ~~In cases where a boundary curve intersected regions lacking~~ When a boundary intersected regions with missing data, local interpolation of the ~~flow~~ velocity field was performed prior to ~~interpolating values~~ interpolation onto the boundary nodes.

To assess sensitivity to the integration contour, the nominal curve dimensions were systematically perturbed by $\pm 5\%$ in both width and height, using ten discrete variations in each direction, yielding an ensemble of 100 contour realisations per curve geometry. Circulation was evaluated for each realisation, with elliptical and rectangular contours treated separately. This procedure was applied identically to both CFD and PIV datasets. A convergence study on lift and circulation, ~~detailed~~ reported in App. E, was ~~conducted to determine appropriate boundary definitions~~used to select the optimal nominal contour dimensions; the final settings are ~~summarized~~ summarised in Table 6. While CFD results ~~demonstrated consistent convergence across boundary~~ showed robust convergence across contour variations, PIV-derived quantities ~~showed greater sensitivity. To reduce variability, circulation values from PIVwere averaged over 100 slightly perturbed boundary sizes for each curve shape~~exhibited greater sensitivity, motivating ensemble averaging. The reported circulation values, therefore, represent identical ensemble averages for CFD and PIV, obtained by averaging over the 100 perturbed contours for each geometry and subsequently between the elliptical and rectangular cases.

The resulting circulation strength Γ distributions obtained from CFD and from PIV, which extend up to section $Y6$, are shown in Fig. 8. ~~For reference, predictions~~ Predictions from novel simulations using the vortex-step method (VSM) at a ~~$\mathrm{Re} = 3.8 \times 10^5$~~ $\mathrm{Re} = 3.8 \times 10^5$ are also included, employing the recommended settings and 2D polars outlined in the companion paper~~(Poland et al., 2025a). Two distinct sources of uncertainty in the circulation measurements are represented by 90% confidence intervals (CIs). The first CI, shown as red-shaded areas, captures uncertainty due to velocity fluctuations across the 250 PIV images and is denoted as $\sigma_{\Gamma,u}$. It is computed as the difference between the circulation~~ (Poland et al., 2025a). For PIV plane $Y7$, the fraction of vectors requiring interpolation within the interpolation squares exceeded 1% for all 100 contour

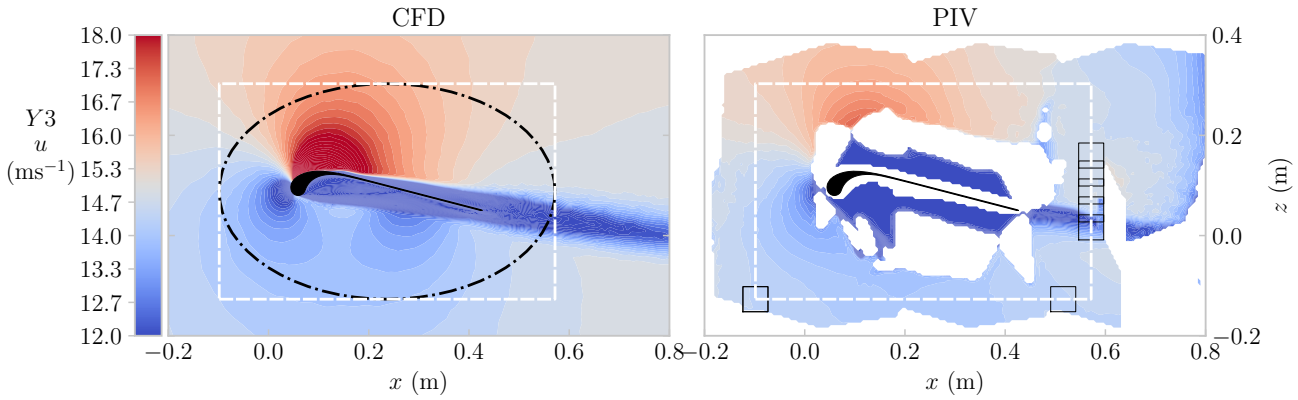

Figure 7. The velocity magnitude field, u, is shown for both CFD (left) and PIV (right) at plane $Y3$ and angle of attack $\alpha = 7°$. On the CFD plot, elliptical and rectangular bound curves are displayed, while the PIV plot features a rectangular bound curve along with interpolation squares.

perturbations (App. E). This plane was therefore omitted from the quantitative analysis. Only $\alpha = 7°$ was analysed as planes $Y2$, $Y3$ and $Y4$ report too high uncertainties, evident from Table 4, 5 and D1 in App. D.

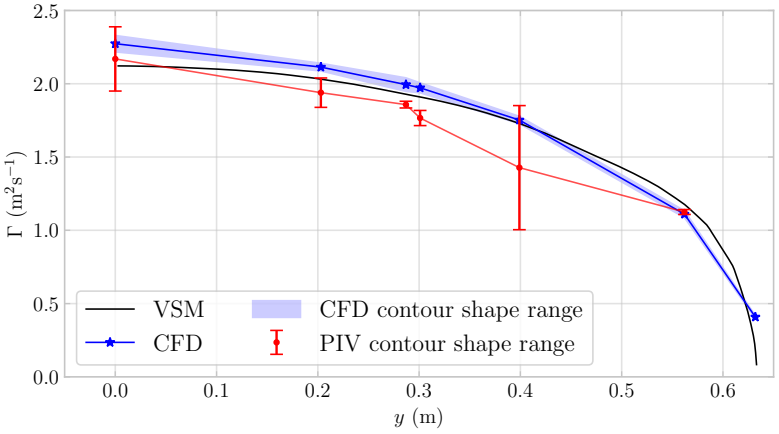

Figure 8. Circulation distribution at $\alpha = 7°$, computed using boundary curve velocity interpolation, is shown for CFD across all measurement planes, for PIV data up to plane $Y6$, and as predicted by the VSM method.

The uncertainty shown in Fig. 8 quantifies the sensitivity of Γ to the integration contour. Elliptical and rectangular contours were evaluated, and, for each shape, Γ was averaged over an ensemble of 100 small contour-size perturbations for both CFD and PIV. The reported value is the mean of the two shape-averaged estimates. The plotted intervals are derived from the ~~mean velocity field and that obtained by perturbing the velocity field by one standard deviation. The second CI accounts for variations~~

~~across the 100 different boundary shapes, denoted as $\sigma_{\Gamma,\mathrm{b}}$. Since these variations represent random approximations of the true circulation boundary, the corresponding standard deviation is scaled by $1/\sqrt{100}$ to reflect the averaging procedure. The total standard deviation σ_Γ, combining contributions from both velocity fluctuations and boundary shape variation, is computed as:~~

~~$\sigma_\Gamma = \sqrt{\sigma_{\Gamma,\mathrm{u}}^2 + \sigma_{\Gamma,\mathrm{b}}^2}.$~~

same contour ensemble in both datasets: PIV is shown with error bars, and CFD with shaded bands, each spanning the full min–max range across the 100 perturbations. Statistical uncertainty associated with finite-sample velocity fluctuations across the 250 PIV realisations contributes an additional 2–10 % for most planes, but is omitted from the plotted intervals to preserve consistency with the CFD presentation.

The small confidence band indicates that CFD-derived circulation distributions using elliptical and rectangular bound shapes were similar, though not identical; the influence of the bound shape diminished toward the wingtip, see Fig. 8. In contrast, PIV measurements were notably more sensitive~~: rectangular contours consistently yielded wider σ_Γ confidence intervals than elliptical ones, indicating greater uncertainty, primarily due to boundary-induced effects. The~~ ; the largest divergence occurred at $Y5$ ($y = 0.399$ m), ~~where both the PIV contour discrepancy and the~~ aligning with where the CFD–PIV mismatch peaked. The increased sensitivity of the PIV-derived circulation at plane $Y5$ coincides with elevated stitching-related velocity offsets in the overlap regions, as quantified in App. D. This reduced inter-plane consistency further limits the robustness of gradient-based quantities at this location. For $Y6$, the smaller spread is a methodological artefact: extensive missing data eliminate many contour realisations, leaving a restricted admissible subset and therefore an artificially reduced ensemble variability. Figure D1 further illustrates why $Y7$ requires excessive interpolation for essentially all contour realisations, and is therefore excluded from the quantitative analysis.

Although RANS-based CFD and the ~~Vortex-Step Method~~ VSM employ different numerical schemes, they predicted similar trends and magnitudes of circulation, verifying the correctness of the integration routine. ~~Up to $Y3$, experimental and numerical circulations aligned-albeit less closely-providing additional validation.~~ The overall agreement in distributed circulation indicates that the numerical tools ~~accurately reproduce the distributed aerodynamic loads, and~~ reproduce the trends in the distributed aerodynamic load. This secondary data source decreases the likelihood that the previously reported integral-lift agreement Poland et al. (2025a) was ~~not a result of~~ due to compensating errors. ~~Circulation distribution at $\alpha = 7°$, computed using boundary curve velocity interpolation, is shown for CFD across all measurement planes, for PIV data up to plane $Y6$, and as predicted by the VSM method.~~

The forces computed using the Kutta–Joukowski equation from circulation, the Noca's method, and pressure integration are ~~summarized~~ summarised in Table 6 for both rectangular and elliptical boundary shapes. Only planes containing sufficient data for boundary curve interpolation are included in the analysis.

~~The Noca-derived values are consistent across both boundary shapes for CFD, whereas PIV results exhibit greater sensitivity to boundary shape, consistent with the circulation findings. Among the tested shapes, the ellipse provides the closest agreement between PIV and CFD, consistent with the smaller confidence intervals shown in Fig. 8. The CFD-derived $C_{\mathrm{l,\,Noca}}$ values at $Y3$ and $Y4$ are nearly identical, reflecting their close spatial proximity. At $Y1$, which has the lowest measurement uncertainty, the~~

~~C_l values obtained using Noca's method are nearly identical for both CFD and PIV. Due to the presence of unphysical negative drag values on some~~ For an overview of all planes, the ~~$C_{d,\text{Noca}}$ results are considered generally unreliable. Nonetheless, at $\alpha = 17°$, the elevated $C_{d,\text{Noca}}$ values are consistent with anticipated and measured increases in 3D integral drag at the same angle of attack (Poland et al., 2025b).~~

~~The non-dimensional force calculated using the Kutta–Joukowski theorem, $C_{l,\text{Kutta}}$, generally exhibits higher values than the reported lift coefficients. The differences between PIV and CFD results, as well as between elliptical and rectangular PIV boundaries, increased progressively towards the wingtip, consistent with previously noted effects of planar misalignment, reduced validity of the 2D assumption, and increasing out-of-plane flow, all contributing to elevated uncertainty. As shown in~~ reader is referred to Fig. ~~8, the PIV ellipse result at $Y5$ deviates from the overall trend, which is reflected in the $C_{l,\text{Kutta}}$ value, but not necessarily observed in $C_{l,\text{Noca}}$ or $C_{d,\text{Noca}}$.~~

~~The pressure integration values are comparable in magnitude to those obtained using Noca's method. However, from $Y1$ to $Y4$, the trend of decreasing aerodynamic performance predicted by Noca's method, the Kutta–Joukowski method, and VSM is not reflected in the pressure integration results. Notably, at $Y4$, both lift and drag increase. Possible causes for this discrepancy are examined in Sect. 4.~~ D1 in App. D.

Table 6. Aerodynamic coefficients for the measured PIV and simulated CFD of different planes, using different calculation methods.

Plane	α	Boundary Setting			Ellipse		Rectangle			P-integration
					CFD	PIV	CFD	PIV		CFD
		x_b, z_b	0.24, 0.14 (m)	$C_{l,\text{Noca}}$ $(-)$	0.60	0.61	0.60	0.39	$C_{l,p}$ $(-)$	0.53
$Y1$	7°	W_b, H_b	0.6, 0.37 (m)	$C_{d,\text{Noca}}$ $(-)$	0.02	0.20	0.02	0.25	$C_{d,p}$ $(-)$	0.02
		N_b	360 $(-)$	$C_{l,\text{Kutta}}$ $(-)$	0.78	0.80	0.74	0.65		
		x_b, z_b	0.24, 0.12 (m)	$C_{l,\text{Noca}}$ $(-)$	0.57	0.43	0.57	0.36	$C_{l,p}$ $(-)$	0.49
$Y2$	7°	W_b, H_b	0.67, 0.39 (m)	$C_{d,\text{Noca}}$ $(-)$	-0.04	0.25	-0.05	0.35	$C_{d,p}$ $(-)$	0.02
		N_b	360 $(-)$	$C_{l,\text{Kutta}}$ $(-)$	0.72	0.68	0.70	0.62		
		x_b, z_b	0.24, 0.09 (m)	$C_{l,\text{Noca}}$ $(-)$	0.53	0.44	0.54	0.39	$C_{l,p}$ $(-)$	0.51
$Y3$	7°	W_b, H_b	0.67, 0.43 (m)	$C_{d,\text{Noca}}$ $(-)$	0.01	0.48	0.01	0.24	$C_{d,p}$ $(-)$	0.03
		N_b	360 $(-)$	$C_{l,\text{Kutta}}$ $(-)$	0.68	0.63	0.65	0.61		
		x_b, z_b	0.24, 0.09 (m)	$C_{l,\text{Noca}}$ $(-)$	0.53	0.51	0.54	0.36	$C_{l,p}$ $(-)$	0.73
$Y4$	7°	W_b, H_b	0.65, 0.42 (m)	$C_{d,\text{Noca}}$ $(-)$	-0.02	0.08	-0.02	0.16	$C_{d,p}$ $(-)$	0.08
		N_b	360 $(-)$	$C_{l,\text{Kutta}}$ $(-)$	0.67	0.61	0.65	0.57		
		x_b, z_b	0.23, 0.16 (m)	$C_{l,\text{Noca}}$ $(-)$	0.48	0.56	0.47	0.30	$C_{l,p}$ $(-)$	0.41
$Y5$	7°	W_b, H_b	0.70, 0.40 (m)	$C_{d,\text{Noca}}$ $(-)$	-0.08	-0.14	-0.08	-0.06	$C_{d,p}$ $(-)$	0.02
		N_b	360 $(-)$	$C_{l,\text{Kutta}}$ $(-)$	0.60	0.34	0.58	0.62		
		x_b, z_b	0.25, 0.09 (m)	$C_{l,\text{Noca}}$ $(-)$	0.57	0.77	0.58	0.77	$C_{l,p}$ $(-)$	0.41
$Y1$	17°	W_b, H_b	0.60, 0.44 (m)	$C_{d,\text{Noca}}$ $(-)$	0.29	-0.29	0.48	0.22	$C_{d,p}$ $(-)$	0.08
		N_b	360 $(-)$	$C_{l,\text{Kutta}}$ $(-)$	0.69	0.82	0.70	0.89		

The Noca-derived values are consistent across both boundary shapes for CFD, whereas PIV results exhibit greater sensitivity to boundary shape, consistent with the circulation findings. Among the tested shapes, the ellipse provides the closest agreement between PIV and CFD. The CFD-derived $C_{\mathrm{l,Noca}}$ values at $Y3$ and $Y4$ are nearly identical, reflecting their close spatial proximity. At $Y1$, which has the lowest measurement uncertainty, the C_{l} values obtained using Noca's method are nearly identical for both CFD and PIV.

Due to the occurrence of negative sectional drag estimates on several planes, the $C_{\mathrm{d,Noca}}$ results are considered generally unreliable. This behaviour is consistent with the well-established difficulty of extracting drag from velocity-field-based force integration, as drag is typically an order of magnitude smaller than lift and therefore highly sensitive to measurement noise, spatial resolution, and systematic bias (Fritz et al., 2024a, b). In addition, drag depends on subtle momentum deficits and viscous contributions in the near and far wake, which are difficult to resolve accurately with planar PIV in the presence of wake truncation, masking, and incomplete near-wall information (Huang et al., 2023). These limitations are further exacerbated by out-of-plane effects, which disproportionately affect drag compared to lift in velocity-only formulations (LeBlanc and Ferreira, 2022).

Nonetheless, at $\alpha = 17°$, the elevated $C_{\mathrm{d,Noca}}$ values are qualitatively consistent with the anticipated and independently measured increase in 3D integral drag at the same angle of attack (Poland et al., 2025b), indicating that while absolute drag levels are unreliable, the method retains sensitivity to gross drag trends at high loading.

The non-dimensional force calculated using the Kutta–Joukowski theorem, $C_{\mathrm{l,Kutta}}$, generally exhibits higher values than the reported sectional lift coefficients. The differences between PIV and CFD results, as well as between elliptical and rectangular PIV boundaries, increased progressively towards the wingtip, consistent with previously noted effects of planar misalignment, reduced validity of the 2D assumption, and increasing out-of-plane flow, all of which contributed to elevated uncertainty. As shown in Fig. 8, the PIV result at $Y5$ deviates from the overall trend, which is reflected in the $C_{\mathrm{l,Kutta}}$ value, but not necessarily observed in $C_{\mathrm{l,Noca}}$ or $C_{\mathrm{d,Noca}}$.

The pressure-integration values are comparable in magnitude to those obtained using Noca's method. However, from $Y1$ to $Y4$, the monotonic decrease in aerodynamic performance predicted by Noca's method, the Kutta-Joukowski method, is not reproduced by the pressure-integration results. Instead, the pressure-based sectional loads exhibit a local off-trend increase at planes $Y3$ and $Y4$, most pronounced at $Y4$, where both lift and drag increase. As these planes coincide with the second strut location, the deviation suggests a local 3D disturbance that violates the assumptions underlying planar sectional analysis and is not captured by circulation- or boundary-curve-based methods. This hypothesis is examined in Sect. 4.3, where CFD data are used to interpret the origin of these deviations.

4 Discussion

This section interprets the experimental findings by addressing ~~critical~~ key aspects of data quality and accuracy, followed by explanations for the observed discrepancies between experimental and numerical results. ~~The section first evaluates~~ It begins by

evaluating the limitations inherent to the PIV measurements, ~~subsequently~~ then discusses quantitative analysis discrepancies, and concludes with an investigation ~~into~~ of local aerodynamic phenomena induced by the wing struts.

4.1 PIV measurement limitations

The ~~raw PIV data showed anomalous regions, particularly near the airfoil surface on both suction and pressure sides. We hypothesize that these anomalies primarily result~~ dominant limitation of the present stereoscopic PIV measurements arises from surface reflections ~~caused by the LEI wing's complex geometry, which includes a double-curved anhedral shape, a near-circular~~ associated with the complex LEI wing geometry, characterised by pronounced anhedral curvature, a near-cylindrical leading edge, and multiple strut elements. ~~This explanation is supported by the increased occurrence of faulty regions in planes $Y3$ and $Y4$, both located near a strut, as shown in Fig. 6. Raw image analysis further reveals a strong spatial correlation between these velocity anomalies and distinct geometric features, reinforcing the conclusion that surface reflections are the dominant source of error~~These reflections lead to local correlation failure and data loss in the vicinity of the airfoil surface, particularly in regions where the laser light sheet impinges at shallow angles. For LEI-type wings with strongly curved leading edges and anhedral canopies, reflection avoidance therefore constitutes a primary experimental constraint, alongside optical access and measurement-plane alignment, and should be prioritised in future PIV campaign designs.

Despite ~~various mitigation efforts, including support-structure masking, matte black spray paint, and dedicated~~ extensive mitigation measures, including matte black surface treatment, masking of support structures, and tailored post-processing, ~~artifacts remained in the data. To mitigate their impact, a lateral velocity u_y filter was applied to exclude visibly faulty regions , as described in App. **??**. However, this filtering did not fully eliminate all anomalies, as indicated by the dark blue regions in Fig. 6. These areas were deemed faulty due to their clear mismatch with CFD results, which display smooth and physically consistent flow. Reflection-induced gaps in the data required interpolation near the surface, introducing localized uncertainties that reduce the fidelity of velocity gradients and derived aerodynamic quantities~~ reflection-induced artefacts could not be fully eliminated. The affected regions necessitated masking and, in some cases, local interpolation of the velocity field, particularly close to the surface. These procedures introduce localised uncertainty and disproportionately affect near-wall velocity gradients, thereby reducing the reliability of derived quantities that depend on spatial derivatives, such as circulation and sectional force estimates.

The impact of these limitations is not uniform across the wing. Toward the tip, increasing geometric curvature leads to greater misalignment between the measurement plane and the local flow direction, amplifying out-of-plane transport and further reducing the validity of psuedo-2D sectional assumptions. Consequently, sectional force estimates in these regions should be interpreted with caution, whereas mid-span planes—where masking and interpolation are limited—provide the most reliable quantitative information.

~~Measurements on both the suction and pressure sides were conducted on the same half of the wing, shown on the left in Fig. 2, thereby avoiding uncertainties related to geometric asymmetries. A randomized convergence study confirmed robust convergence of mean velocities over the 250-image sequence, see Fig. A1 in App. A.~~ Overall, while the measured flow fields robustly capture the dominant flow topology and spanwise trends, surface-adjacent quantities and gradient-based load estimates

remain sensitive to reflection-induced data loss and measurement-plane misalignment. These limitations define the practical bounds within which the present PIV dataset can be interpreted quantitatively.

~~Despite mitigation efforts, anomalous regions persisted and required interpolation , particularly near the airfoil surface, introducing localized uncertainties that reduce the fidelity of near-wall velocity gradients and , consequently, compromise the accuracy of aerodynamic force estimates .~~

4.2 Quantitative analysis discrepancies

Incomplete velocity data near the airfoil surface necessitated interpolation to enable boundary curve analysis, inherently introducing uncertainty. This limitation is reflected in the sensitivity to boundary curve parameter selection, as demonstrated in App. E in Fig. E2. Averaging across a 10% parameter range reduced variability but did not fully eliminate it. ~~Planes requiring minimal interpolation yielded the closest agreement in lift coefficient between PIV and CFD, see Table 6. In contrast, drag coefficients were less consistent and occasionally resulted in non-physical negative values.~~

In addition to interpolation-related effects, discrepancies may have also been introduced by the integration methods themselves. At $\alpha = 17°$, the 2D planar PIV-derived lift exceeded the ~~CFD-predicted value—opposite to the trend observed in the 3D integrated force measurements reported~~ CFD prediction. This trend contrasted with the 3D-integrated force measurements in the companion paper (Poland et al., 2025b), where CFD produced higher lift. While this discrepancy likely reflects increased uncertainty at high angles of attack, it also suggests ~~the presence of~~ integration errors, as the trend was consistently observed in both ~~Noca's-~~ Noca- and Kutta–Joukowski-based force estimates.

To independently assess aerodynamic loads, surface pressure integration was conducted, incorporating both pressure forces F_{p} and viscous forces $F_{\mathrm{v,j}}$. Pressure forces dominated, with viscous contributions typically below 1%. Compared to values derived from boundary curves, see Table 6, the pressure integration results showed different magnitudes but similar trends, except at planes $Y3$ and $Y4$, where elevated lift and drag were observed. For $Y4$, the elevated values are partly attributed to the integration plane intersecting the strut section, which increases the effective airfoil thickness, shown in Fig. 6, thereby enhancing local camber. Supporting this interpretation is the observation that the discrepancy in trend is not captured by the bound integration methods. A further contribution could stem from a local strut effect, which, although smaller than at $Y4$, may also contribute to the off-trend increase in lift and drag observed at $Y3$.

4.3 Local strut effects

The following analysis addresses the off-trend sectional loads observed at planes $Y3$ and $Y4$, which coincide with the second strut location and are not reproduced by velocity-based methods. Because near-wall PIV data in the strut vicinity are insufficient to resolve the associated 3D flow, CFD results are used here solely to interpret the physical origin of these deviations.

In the literature, CFD simulations have been performed both with struts (Viré et al., 2022) and without (Viré et al., 2020). Based on comparisons of global aerodynamic properties, it was concluded that the presence of struts has little influence on overall performance. However, Viré et al. (2022) noted that struts do affect the local flow field, including increased vortex shedding. This observation was supported by spanwise plots of the λ_2-criterion, which provides an indication of vortex core lines in

(Jeong and Hussain, 1995). For the case $\alpha = 13°$ at a ~~$Re = 30 \times 10^5$~~ $Re = 30 \times 10^5$, developing vorticity was found on the pressure side, with structures present between $x/c = 0.3$ and $x/c = 0.6$, except near the tip vortex and the strut regions—indicative of strut-induced effects. The work of Viré et al. (2022) is the published version of the MSc thesis by Lebesque (2020), which further reported that strut blockage influenced the location and size of recirculation regions and, more generally, introduced stronger local effects.

To investigate the mechanism behind the strut-induced effect, measurement planes $Y3$ and $Y4$ were positioned at the location of the second strut. While the flow fields are not resolved close enough to the surface to investigate this mechanism using PIV, CFD results do provide sufficient resolution. As shown in App. ~~??~~ C in Fig. C2, the struts indeed appear to affect the local spanwise flow, evidenced by ~~localized~~ localised regions of increased and decreased u_y values, indicative of a strut-induced velocity increase. This interaction does not produce a uniform effect along the streamwise direction but develops progressively, particularly within the recirculation zone aft of the leading-edge tube.

To investigate this effect, four spanwise slices focused on the second strut, spanning from $x/c = 0.1$ to 0.3, are shown in Fig. 9. The first row displays the streamwise velocity u, where regions of increased upstream flow around the strut are indicated by blue contours. This corresponds to an increase in downward velocity u_z, also shown in blue in the second row, and enhanced spanwise velocity u_y, shown in red in the third row. Similar to the u component, the velocity differences in u_y and u_z become less pronounced downstream, as evident in the last column. ~~The combination of increased downward, sideways~~Near the strut, the flow accelerated downward, spanwise, and upstream~~flow near the strut suggests the presence of a tilted or angled~~ . This combined signature was consistent with a tilted vortex structure.

To investigate whether vortices are present, the λ_2 criterion is plotted in the last row. It is derived from the eigenvalues of the symmetric tensor $\mathbf{E}^2 + \mathbf{W}^2$, where the square denotes a matrix multiplication yielding another second-order tensor. The symmetric strain rate and antisymmetric spin tensors are defined as

$$\mathbf{E} = \frac{1}{2}\left(\nabla\mathbf{u} + (\nabla\mathbf{u})^\mathsf{T}\right), \quad \text{and} \tag{11}$$

$$\mathbf{W} = \frac{1}{2}\left(\nabla\mathbf{u} - (\nabla\mathbf{u})^\mathsf{T}\right), \tag{12}$$

respectively, where $\nabla\mathbf{u}$ denotes the velocity gradient tensor.

The λ_2 criterion specifically evaluates the second-largest eigenvalue of this tensor, where $\lambda_2 < 0$ indicates the presence of a vortex core (Jeong and Hussain, 1995). The values reported here differ in magnitude from those in Viré et al. (2022) due to the adjustment in angle of attack, scaling to the projected frontal area rather than the projected side area, and the omission of the sign inversion applied in that study.

At $x/c = 0.1$, the λ_2-criterion indicates negative regions within the shear layer and close to the surface on the outward side of the strut. The latter region somewhat corresponds to areas of elevated u_y and u_z velocities. Closer to the strut, the shear layer structures begin to break down. The breaking down phenomenon intensifies downstream and coincides with a shear layer bump best observed in the u velocity plot, attributed to negative u_y regions. Another factor contributing to the breakdown of a well moving downstream is increased turbulent mixing. By $x/c = 0.3$, a region of negative λ_2 values has grown in size and now covers nearly the entire recirculation region.

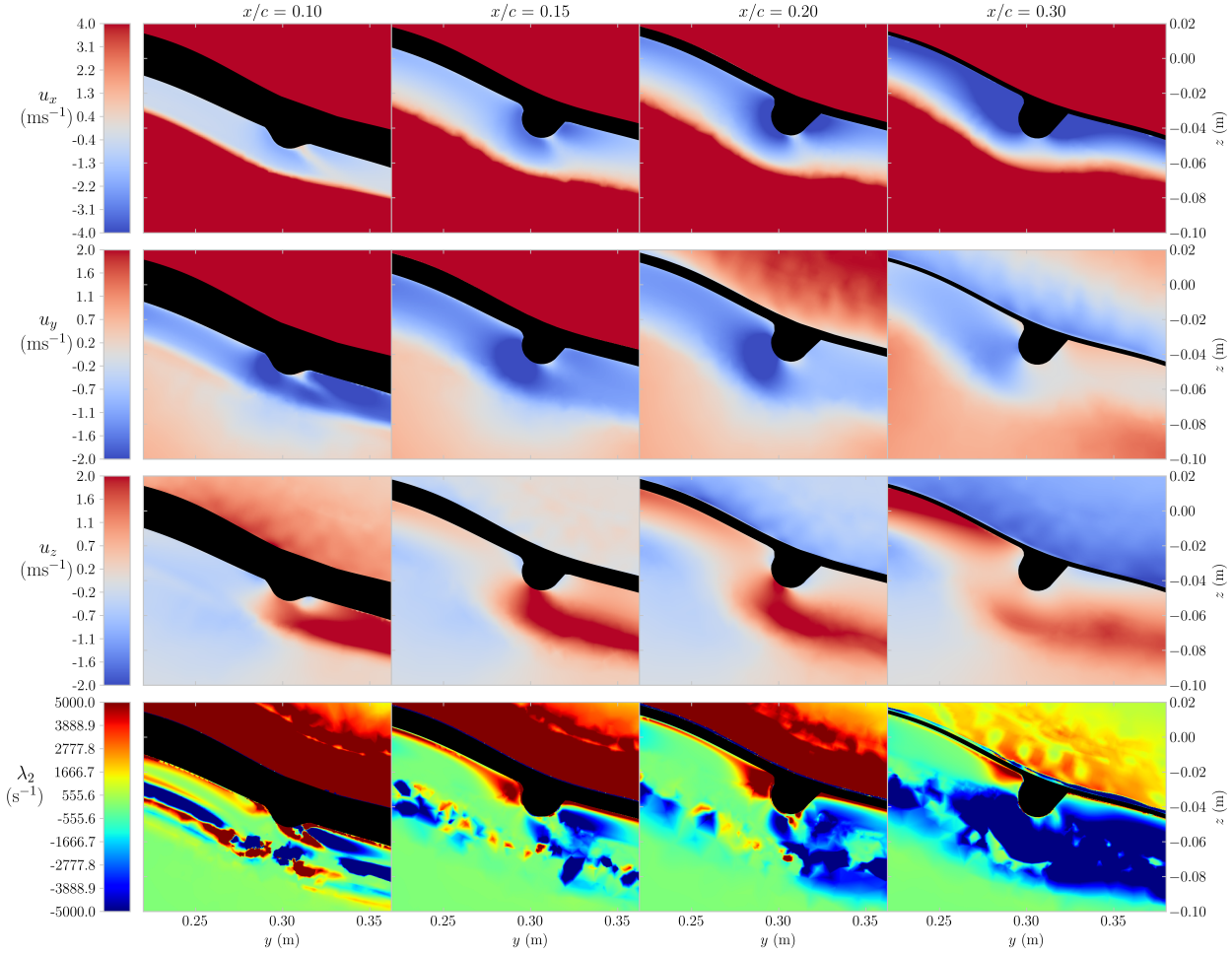

Figure 9. Spanwise CFD slices at $\alpha = 7°$ and $\mathrm{Re} = 10 \times 10^5$ near the second strut. Columns show four x/c locations; rows show u_x, u_y, u_z, and λ_2. Upstream slices intersect the leading-edge tube and fillet, so the membrane is only visible at the most downstream location.

In summary, the strut ~~induces a local increase in flow~~ is associated with local increases in velocity in all three spatial directions, ~~indicating~~ consistent with a strong 3D interaction. This effect cannot be attributed solely to spanwise ~~2D flow components~~transport, as elevated upstream velocities in the u direction ~~were also observed within~~ are also observed in the strut region. ~~These features suggest the presence of~~ The combined signatures are consistent with a 3D mechanism, such as an ~~angled~~ inclined vortex originating near the inward ~~tip side , that may~~ side of the strut, which could account for the ~~observed~~ local upstream flow. Although the upstream shear layer is clearly ~~defined~~ identified in the λ_2 ~~plot~~field, the existence and topology of such a vortex ~~could not be definitively confirmed .~~ cannot be confirmed unambiguously from the present evidence.

Nevertheless, the strut's influence on both velocity and vorticity shedding is apparent. Given the spatial overlap between these disturbed flow regions and planes $Y3$ and $Y4$, the strut effect is a credible contributor to the elevated lift and drag observed in the surface pressure integration. While global aerodynamic coefficients remain largely unaffected by strut inclusion, as reported by (Viré et al., 2022), this CFD analysis demonstrates how the struts affect local aerodynamic phenomena, highlighting important implications for both experimental interpretation and sectional load ~~modeling~~modelling. ~~Spanwise CFD slices were generated at $\alpha = 7°$ and a Re $= 10 \times 10^5$. The columns show different x/c locations, indicating the development of the recirculation zone flow near the strut. The first columns intersect part of the leading-edge tube and fillet, and therefore do not capture the thin membrane, which becomes visible in the final column. The rows indicate the three flow velocity components u_x, u_y, and u_z, and the last row shows the λ_2-criterion.~~

5 Conclusion

~~A novel stereoscopic particle image velocimetry (PIV) campaign was conducted in the Open-Jet Facility at TU Delft on a rigid 1:6.5~~

This study has presented the first geometry-consistent, spatially resolved stereoscopic PIV dataset for a representative LEI kite configuration, obtained from a rigid 1:6.5 scale model of the TU Delft V3 ~~leading-edge inflatable (LEI) kite . The addition of this experimentally measured flow-field dataset reinforces the model's status as a benchmark configuration for LEI kites. The experiments used the same idealized geometry with fillets as employed in simulations to ensure consistency in comparison.~~ kite in controlled wind-tunnel conditions. By combining stereoscopic PIV measurements with RANS simulations and vortex-step-method predictions, the work addresses a previously unresolved gap in the experimental characterisation of sectional flow physics for strongly anhedral, double-curved kite wings.

The ~~complex LEI wing geometry, including its double-curved anhedral canopy, near-cylindrical leading edge, and struts, includes surfaces that often face directly toward the laser light sheet, making them particularly prone to unwanted reflections. As a result, the authors hypothesize that reflections were the dominant source of anomalous velocity vectors in the PIV images. Despite the use of matte coatings, masked regions, and tailored processing, these effects remained significant, highlighting the need for further refinement of reflection suppression techniques~~ stereoscopic PIV fields reproduce the dominant CFD-predicted topology, including suction-side acceleration and stall-associated shear-layer development at elevated angles of attack. Circulation distributions from bound-curve integration show consistent spanwise trends between PIV, CFD, and VSM predictions at

$\alpha = 7°$, supporting numerically predicted sectional loading trends and indicating robustness of circulation-based metrics under the present pseudo-2D assumption when out-of-plane transport is limited. The closest quantitative agreement between PIV and CFD in sectional lift is obtained at mid-span, where measurement-plane alignment is most favourable and reflection-induced data loss is minimal.

By contrast, drag recovery from near-field planar velocity data is shown to be fundamentally unreliable in the present configuration. Negative or non-physical sectional drag estimates arise from the combined effects of near-wall data loss, wake truncation, sensitivity to velocity gradients, and unaccounted three-dimensional momentum transport. These findings reinforce the established limitation of velocity-field-based drag estimation and delineate the practical bounds within which planar PIV-derived force estimates can be interpreted for LEI wings.

~~Qualitatively, the PIV vector maps reproduce the principal flow-field features predicted by computational fluid dynamics (CFD), with velocity fields showing consistent magnitudes, particularly at an angle of attack of 17° in the wake and separated flow regions that are minimally affected by surface reflections. The location of stall onset, previously inferred only from~~ Local offsets between adjacent PIV planes are consistent with strut-induced three-dimensional ~~(3D) integral load trends, was thus directly confirmed in the measurements, reinforcing the reliability of both methods in capturing key flow phenomena at high angles of attack~~disturbances that violate the pseudo-two-dimensional assumption. CFD indicates local acceleration and vorticity redistribution in the strut vicinity, which can perturb sectional loads without materially affecting global coefficients and thereby limits the interpretability of planar force estimates near the struts.

~~Although surface-adjacent flow could not be fully resolved and some anomalous regions remained, quantitative comparison based on bound-curve integration remained feasible. Spanwise circulation extracted from the PIV measurements aligns well with both CFD and vortex step method predictions. Furthermore, loads derived from two-dimensional momentum integration of the measurements show good agreement with CFD, particularly when elliptical integration boundaries are applied at mid-span, where uncertainty was lowest.~~ Overall, the dataset supports model–experiment comparison of mean-flow topology and spanwise circulation trends in planes with sufficient data coverage. Where plane alignment is favourable and masking is limited (close to mid-span), pseudo-two-dimensional sectional lift estimates are broadly consistent with CFD. Limitations due to near-surface data loss, drag-recovery sensitivity, and strongly three-dimensional regions are quantified and explicitly documented. In this sense, the work provides benchmark data and an explicit applicability map for the presented measurement approach.

~~Beyond validation, the numerical CFD analysis further indicates that the strut accelerates the local flow both spanwise and upstream, enlarging the downstream recirculation zone and redistributing shear-layer vorticity. This highlights the role of strut aerodynamics as a non-negligible factor in sectional load modeling and future kite wing planform optimization.~~

Future ~~efforts are strongly encouraged to explore more effective methods for minimizing reflections, such as advanced coating solutions with ultra-low reflectivity. Implementing a volumetric measurement approach could enable the capture of more 3D effects, including~~ work should prioritise mitigating reflection-induced data loss through improved surface treatments and optical access. Volumetric PIV would enable direct quantification of out-of-plane transport and strut-induced interactions~~.~~ ~~Additional insight may also be gained by analyzing the wake region, particularly the dynamics of tip vortices. Measurement~~

~~quality could be further improved by employing a narrower laser light sheet to concentrate laser power, potentially reducing reflection intensity.~~ , while complementary wake measurements would strengthen the assessment of induced velocities and tip-vortex dynamics. Together, these developments would extend the utility of the TU Delft V3 kite reference dataset for validating flow-resolved aerodynamic models.

Code and data availability. The processed PIV measurements are available on Zenodo from https://doi.org/10.5281/zenodo.17395913. The code for the analysis of this data and the generation of the tables and diagrams in this paper is available on Zenodo from https://doi.org/10.5281/zenodo.17396075 and GitHub from https://github.com/jellepoland/kite_piv_analysis. The CFD data, presented in Viré et al. (2022), and used throughout this study is also available on Zenodo from https://doi.org/10.5281/zenodo.17395314. This code also includes vortex-step method (VSM) simulations, which were performed in the context of this study. The latest version of the VSM can be found on: https://github.com/awegroup/Vortex-Step-Method. The geometric mesh of the TU Delft V3 kite is available on Zenodo from https://doi.org/10.5281/zenodo.15316036 and GitHub from https://github.com/awegroup/TUDELFT_V3_LEI_KITE. More information on the TU Delft V3 Kite is available from https://awegroup.github.io/TUDELFT_V3_KITE/.

Author contributions. JAWP wrote the manuscript, co-designed the experiment, executed the experiment, and performed the analysis. EF co-designed the experiment, executed the experiment, aided in performing the analysis, and made several other contributions to the manuscript. RS supervised the project and made several contributions to the manuscript.

Competing interests. At least one of the (co-)authors is a member of the editorial board of Wind Energy Science.

Acknowledgements. The authors would like to thank the following people for their help: Mark van Spronsen for aiding in data gathering and co-designing the experiment. David Bensason for setting up the PIV and Frits Donker Duyvis for aiding with the laser and more. Mac Gaunaa, Andrea Sciacchitano, and Delphine de Tavernier for advice and guidance.

Financial support. This research has been supported by the Nederlandse Organisatie voor Wetenschappelijk Onderzoek (NWO) under grant number 17628. This work has partially been supported by the MERIDIONAL project, which receives funding from the European Union's 410 Horizon Europe Programme under the grant agreement No. 101084216. We acknowledge the use of OpenAI's ChatGPT and Grammarly for assistance in refining the writing style of this manuscript.

Appendix A: ~~Noca's method, in reduced form~~Convergence over the 250 image samples

This appendix assesses whether the ensemble size of $N = 250$ image pairs is sufficient to obtain statistically converged time-averaged velocities. A representative high-variance case was selected by considering plane $Y4$ at $\alpha = 17°$, which exhibits the largest expanded Type-A uncertainties of the mean among the retained datasets (Table 5). Time series of the instantaneous velocity components u_x, u_y, and u_z at a fixed grid point are shown in Fig. A1. To avoid visual misinterpretation associated with acquisition order, the $N = 250$ samples were randomly permuted prior to plotting.

The monitored point is located above the airfoil surface and corresponds to image-plane coordinates $x = -0.75\,\mathrm{mm}$ and $z = -118.18\,\mathrm{mm}$, i.e. approximately $x \approx 0.25\,\mathrm{m}$ and $z \approx 0.25\,\mathrm{m}$ in the reference frame used throughout the manuscript (cf. Fig. 6). The observed fluctuations remain bounded about a stable mean without systematic drift, indicating that the time-averaged velocity estimate at this location is statistically converged for $N = 250$ samples. Accordingly, the uncertainty metric in Eq. (10) is interpreted as a Type-A (precision) uncertainty of the mean due to finite ensemble size, rather than as evidence of unresolved non-stationarity.

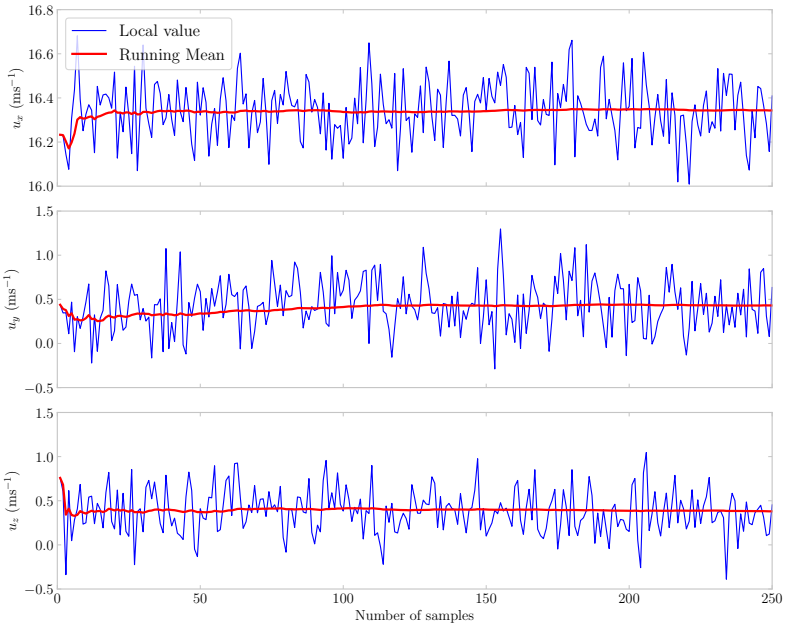

Figure A1. Instantaneous velocity components u_x, u_y, and u_z at a fixed point above the airfoil surface in plane $Y4$ at $\alpha = 17°$. The $N = 250$ samples are randomly permuted for visualisation.

Appendix B: Noca's method, in reduced form

Noca et al. (1999) presented a 3D method for the computation of forces from a boundary surface, given sufficient flow-field information. In the present work, this method was applied under the assumption of 2D incompressible flow. To reduce the

dimensions $\mathcal{N}$ from three to two, a zero was substituted in the second component of the normal vector,

$$\mathbf{n} = \begin{bmatrix} n_x & 0 & n_z \end{bmatrix}^\top, \tag{B1}$$

the position vector,

$$\mathbf{x} = \begin{bmatrix} x & 0 & z \end{bmatrix}^\top, \tag{B2}$$

and the velocity vector,

$$\mathbf{u} = \begin{bmatrix} u_x & 0 & u_z \end{bmatrix}^\top, \tag{B3}$$

and the first and last components of the vorticity vector,

$$\boldsymbol{\omega} = \begin{bmatrix} 0 & \omega_y & 0 \end{bmatrix}^\top. \tag{B4}$$

As shown in Sect. 2.7, the second and third terms of Noca's equation, Eq. (7), fall away: the second term, representing momentum flux through the solid, impermeable surface, is zero due to the no-throughflow condition, and the third term, accounting for boundary acceleration, is zero since the body was stationary. In addition, ~~the steady-flow assumption renders the~~ because the reduced formulation is evaluated using time-averaged, statistically steady fields, the explicit time-derivative terms in the flux equation ~~, corresponding to the~~ (second line of Eq. (8)~~, equal to zero~~) vanish in the formulation used here.

To derive the reduced form, the expressions were rewritten in matrix notation. A direct transfer of the symbolic ordering was not possible, since the left-hand side required a column vector, whereas the right-hand side produced a row vector. This inconsistency was resolved by reordering the dot product, placing the flux term before the surface normal,

$$\frac{\mathbf{F}}{\rho} = \oint_S \gamma_{\text{flux}} \mathbf{n} \mathrm{d}s. \tag{B5}$$

Such a reordering is permissible without modification for symmetric dyadics, but non-symmetric dyadics, present at the third, fourth, and ninth terms, had to be explicitly rewritten by taking the transpose.

B1 Inviscid terms

The first four terms are the inviscid contributions. The first was reduced to

$$\frac{1}{2}\oint_S (u^2\mathbf{I})\mathbf{n}\mathrm{d}s = \frac{1}{2}\oint_S \left((u_x^2+u_z^2) \begin{bmatrix} 1 & 0 & 0 \\ 0 & 1 & 0 \\ 0 & 0 & 1 \end{bmatrix} \right) \begin{bmatrix} n_x \\ 0 \\ n_z \end{bmatrix} \mathrm{d}s = \frac{1}{2}\oint_S \begin{bmatrix} n_x(u_x^2+u_z^2) \\ 0 \\ n_z(u_x^2+u_z^2) \end{bmatrix} \mathrm{d}s, \tag{B6}$$

the second to

$$-\oint_S (\mathbf{u}\mathbf{u}^\top)\mathbf{n}\mathrm{d}s = -\oint_S \left(\begin{bmatrix} u_x \\ 0 \\ u_z \end{bmatrix} \begin{bmatrix} u_x & 0 & u_z \end{bmatrix} \right) \begin{bmatrix} n_x \\ 0 \\ n_z \end{bmatrix} \mathrm{d}s = -\oint_S \begin{bmatrix} n_x u_x^2 + n_z u_z u_x \\ 0 \\ n_x u_x u_z + n_z u_z^2 \end{bmatrix} \mathrm{d}s, \tag{B7}$$

the third to

$$-\frac{1}{\mathscr{N}-1}\oint_S \left[(\mathbf{x}\times\boldsymbol{\omega})\mathbf{u}^\top\right]\mathbf{n}\mathrm{d}s = -\oint_S \left(\begin{bmatrix}-z\omega_y\\0\\x\omega_y\end{bmatrix}\begin{bmatrix}u_x & 0 & u_z\end{bmatrix}\right)\begin{bmatrix}n_x\\0\\n_z\end{bmatrix}\mathrm{d}s = \oint_S \begin{bmatrix}(n_x u_x + n_z u_z)z\omega_y\\0\\-(n_x u_x + n_z u_z)x\omega_y\end{bmatrix}\mathrm{d}s. \tag{B8}$$

and the fourth to

$$\frac{1}{\mathscr{N}-1}\oint_S \left[(\mathbf{x}\times\mathbf{u})\boldsymbol{\omega}^\top\right]\mathbf{n}\mathrm{d}s = \oint_S \left(\begin{bmatrix}0\\xu_z - zu_x\\0\end{bmatrix}\begin{bmatrix}0 & \omega_y & 0\end{bmatrix}\right)\begin{bmatrix}n_x\\0\\n_z\end{bmatrix}\mathrm{d}s = \begin{bmatrix}0\\0\\0\end{bmatrix}. \tag{B9}$$

B2 Viscous terms

The last line of Eq. (8) contains the viscous terms, where the viscous stress tensor $\boldsymbol{\tau}$ appears. Defined in Cartesian coordinates, it was reduced to

$$\boldsymbol{\tau} = \mu\begin{bmatrix}2\frac{\partial u_x}{\partial x}-\frac{2}{3}(\nabla\cdot\mathbf{u}) & \frac{\partial u_x}{\partial y}+\frac{\partial u_y}{\partial x} & \frac{\partial u_x}{\partial z}+\frac{\partial u_z}{\partial x}\\ \frac{\partial u_y}{\partial x}+\frac{\partial u_x}{\partial y} & 2\frac{\partial u_y}{\partial y}-\frac{2}{3}(\nabla\cdot\mathbf{u}) & \frac{\partial u_y}{\partial z}+\frac{\partial u_z}{\partial y}\\ \frac{\partial u_z}{\partial x}+\frac{\partial u_x}{\partial z} & \frac{\partial u_z}{\partial y}+\frac{\partial u_y}{\partial z} & 2\frac{\partial u_z}{\partial z}-\frac{2}{3}(\nabla\cdot\mathbf{u})\end{bmatrix} = \mu\begin{bmatrix}2\frac{\partial u_x}{\partial x} & 0 & \frac{\partial u_x}{\partial z}+\frac{\partial u_z}{\partial x}\\ 0 & 0 & 0\\ \frac{\partial u_z}{\partial x}+\frac{\partial u_x}{\partial z} & 0 & 2\frac{\partial u_z}{\partial z}\end{bmatrix}, \tag{B10}$$

and its divergence becomes

$$\nabla\cdot\boldsymbol{\tau} = \mu\begin{bmatrix}2\frac{\partial^2 u_x}{\partial x^2}+\frac{\partial^2 u_z}{\partial x\partial z}+\frac{\partial^2 u_x}{\partial z^2}\\ 0\\ \frac{\partial^2 u_x}{\partial x\partial z}+\frac{\partial^2 u_z}{\partial x^2}+2\frac{\partial^2 u_z}{\partial z^2}\end{bmatrix} = \mu\begin{bmatrix}\Pi_1\\0\\\Pi_3\end{bmatrix}. \tag{B11}$$

Substituting the reduced forms into the eighth term gives

$$\frac{1}{\mathscr{N}-1}\oint_S \left[\left(\mathbf{x}^\mathsf{T}(\nabla\boldsymbol{\tau})\right)\mathbf{I}\right]\mathbf{n}\mathrm{d}s = \mu\oint_S \left(\begin{bmatrix}x & 0 & z\end{bmatrix}\begin{bmatrix}\Pi_1\\0\\\Pi_3\end{bmatrix}\right)\mathbf{I}\begin{bmatrix}n_x\\0\\n_z\end{bmatrix}\mathrm{d}s = \mu\oint_S \begin{bmatrix}n_x(x\Pi_1+z\Pi_3)\\0\\n_z(x\Pi_1+z\Pi_3)\end{bmatrix}\mathrm{d}s. \tag{B12}$$

The ninth term is reduced to

$$-\frac{1}{\mathscr{N}-1}\oint_S \left[(\nabla\boldsymbol{\tau})\mathbf{x}^\mathsf{T}\right]\mathbf{n}\mathrm{d}s = -\mu\oint_S \left(\begin{bmatrix}\Pi_1\\0\\\Pi_3\end{bmatrix}\begin{bmatrix}x & 0 & z\end{bmatrix}\right)\begin{bmatrix}n_x\\0\\n_z\end{bmatrix}\mathrm{d}s = -\mu\oint_S \begin{bmatrix}\Pi_1(xn_x+zn_z)\\0\\\Pi_3(xn_x+zn_z)\end{bmatrix}\mathrm{d}s. \tag{B13}$$

Finally, the tenth term became

$$\oint_S \boldsymbol{\tau}\mathbf{n}\mathrm{d}s = \mu \oint_S \begin{bmatrix} 2\frac{\partial u_x}{\partial x} & 0 & \frac{\partial u_x}{\partial z}+\frac{\partial u_z}{\partial x} \\ 0 & 0 & 0 \\ \frac{\partial u_z}{\partial x}+\frac{\partial u_x}{\partial z} & 0 & 2\frac{\partial u_z}{\partial z} \end{bmatrix} \begin{bmatrix} n_x \\ 0 \\ n_z \end{bmatrix} \mathrm{d}s = \mu \oint_S \begin{bmatrix} n_x\left(2\frac{\partial u_x}{\partial x}\right)+n_z\left(\frac{\partial u_x}{\partial z}+\frac{\partial u_z}{\partial x}\right) \\ 0 \\ n_x\left(\frac{\partial u_z}{\partial x}+\frac{\partial u_x}{\partial z}\right)+n_z\left(2\frac{\partial u_z}{\partial z}\right) \end{bmatrix} \mathrm{d}s. \tag{B14}$$

B3 Reduced form

Combining everything, the following reduced form was obtained:

$$\begin{aligned} \frac{F_x}{\rho} = \oint_S \Bigg[& \frac{1}{2}n_x\left(u_z^2-u_x^2\right) - n_z u_x u_z + (n_x u_x + n_z u_z) z\omega_y + \mu n_x(x\Pi_1 + z\Pi_3) - \mu\Pi_1(xn_x + zn_z) \\ & + \mu\left(2n_x\frac{\partial u_x}{\partial x} + n_z\left(\frac{\partial u_x}{\partial z}+\frac{\partial u_z}{\partial x}\right)\right)\Bigg]\mathrm{d}s, \\ \frac{F_z}{\rho} = \oint_S \Bigg[& \frac{1}{2}n_z\left(u_x^2-u_z^2\right) - n_x u_x u_z - (n_x u_x + n_z u_z) x\omega_y + \mu n_z(x\Pi_1 + z\Pi_3) - \mu\Pi_3(xn_x + zn_z) \\ & + \mu\left(n_x\left(\frac{\partial u_x}{\partial z}+\frac{\partial u_z}{\partial x}\right) + 2n_z\frac{\partial u_z}{\partial z}\right)\Bigg]\mathrm{d}s, \end{aligned} \tag{B15}$$

with

$$\Pi_1 = 2\frac{\partial^2 u_x}{\partial x^2} + \frac{\partial^2 u_z}{\partial x \partial z} + \frac{\partial^2 u_x}{\partial z^2}, \qquad \Pi_3 = \frac{\partial^2 u_x}{\partial x \partial z} + \frac{\partial^2 u_z}{\partial x^2} + 2\frac{\partial^2 u_z}{\partial z^2}. \tag{B16}$$

Appendix C: Masking

The three velocity components u_x, u_y and u_z of plane $Y1$, unmasked and masked are shown in Fig. C1. The raw u_y ~~component plot reveals areas with unrealistically high~~ field contains spatially localised regions with unrealistically large out-of-plane velocities~~that are not expected in the symmetry plane of the wing . The color~~ . In the present measurement planes, values with $|u_y| > 3\ \mathrm{ms}^{-1}$ are inconsistent with the corresponding CFD predictions and occur predominantly in zones affected by surface reflections and correlation loss. The applied threshold is therefore introduced as a reconstruction-failure proxy to suppress reflection-driven artefacts, rather than as a physical constraint on genuine 3D flow (e.g. near the wing tip or strut junctions). The colour bar is limited to $\pm 3\ \mathrm{ms}^{-1}$ for better interpretability. The u_x and u_y velocity components in the same areas also exhibit unrealistic values. Comparisons with raw images revealed that reflections in these areas prohibited accurate PIV processing. This led to the conclusion that the discussed regions require a masking procedure.

Using the standard deviation as a mask to remove these regions proved ineffective because it could not capture all the zones and removed many data points outside the identified regions. This was especially prevalent in the α = 17° case, where a large separated flow region is present that, given its unsteady nature, fluctuates substantially over the 250 images, thereby causing large standard deviations that would have consequently been filtered out. The lateral velocity component u_y provided the best

proxy to filter out the data points, which also removed most of the off-predicted u_x and u_z regions due to the overlap with the off-predicted u_y regions.

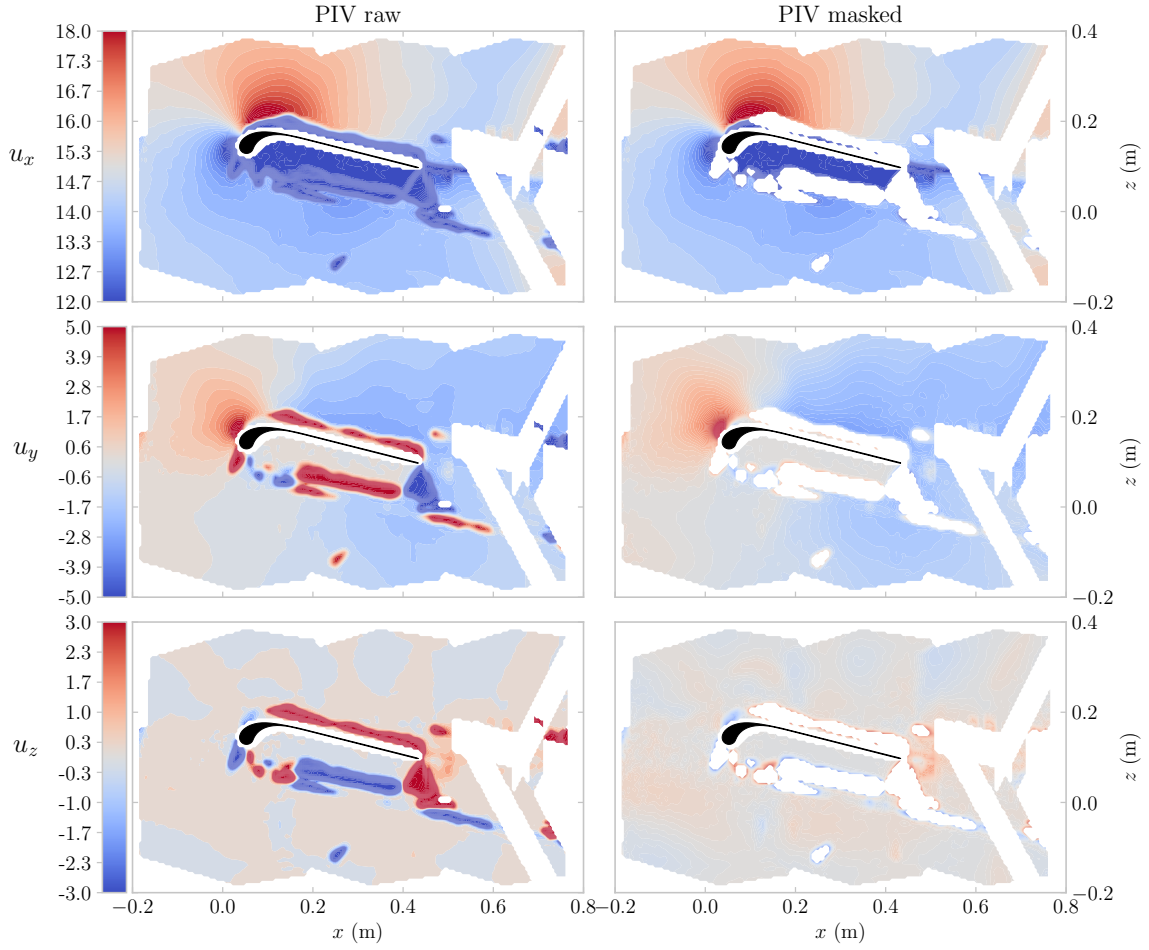

Figure C1. The first column indicates the unmasked raw PIV images for the three velocity components u_x, u_y and u_z at measurement plane $Y1$ and ~~α is 6~~$\alpha = 7°$. The second column shows the same plane, but masked using a ~~u_z~~ u_y filter.

755 Both the identification of regions as off-prediction and selecting $\pm$ 3 ms^{-1} u_y to mask the experimental data were motivated by comparing the measured data to numerical data. Two spanwise slices are plotted in Fig. C2, which show that no u_y components outside of $\pm$ 3 ms^{-1} range are present for the measurement planes, except the $Y7$ plane for the ~~$\alpha = 6$~~$\alpha = 7°$ case. With

α = 17°, a larger white region shows but does not cross any of the measurement planes, i.e., at this α, only up to $Y4$ located at $y = 0.301$ m, measured were made.

An additional mask was applied to exclude the regions where the support structure holding the wing obstructed the camera's line of sight and, thus, prohibited particle tracking. These masked areas are visible behind the wing's trailing edge, see Fig. C1.

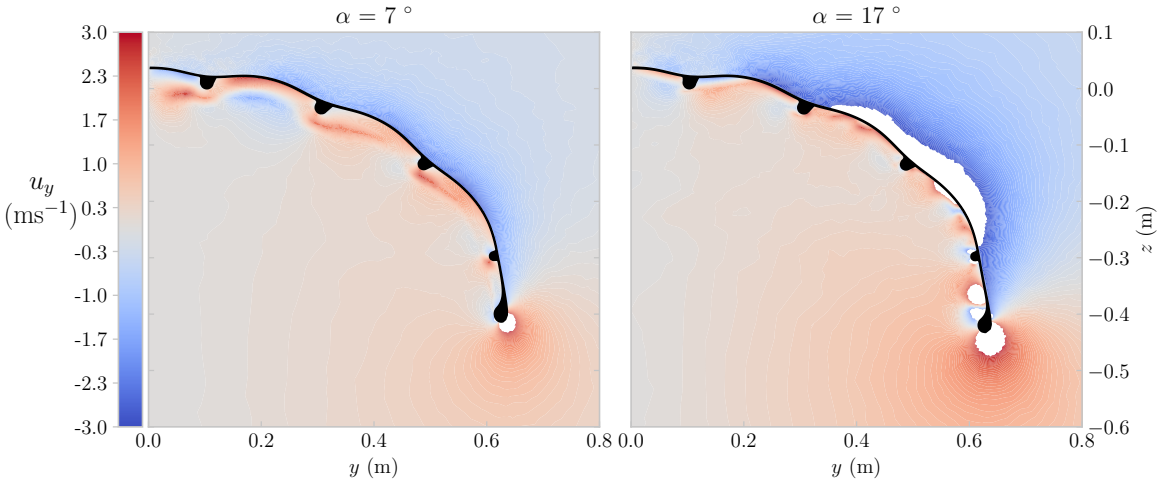

Figure C2. Spanwise slices of the u_y flow fields made using the data from Viré et al. (2022), the left showing the α = 7° case and the right the 17° case. The white regions indicate where the absolute u_y velocity is larger than 3 ms^{-1}. The displayed slices are taken at 0.25 x/c offset from the leading edge in the stream-wise x direction.

Appendix D: Stitching uncertainty

To quantify the consistency between adjacent PIV sub-planes after stitching, a stitching uncertainty was evaluated from the velocity differences in the overlap regions. However, missing vectors and locally degraded reconstruction quality in the overlap regions reduced the spatial coverage available for these comparisons and prevented robust averaging over the full overlap extents. Therefore, the reported stitching uncertainty was computed from a restricted subset of overlap points sampled above an upper-layer line at $z = 0.25$ m. This line was selected because, for the measurement planes emphasised in the manuscript, and for those with comparatively lower uncertainty (Table 5), the reconstructed flow fields in this region remained qualitatively consistent. The measured velocity fields and the corresponding line used for the overlap analysis are shown in Fig. D1.

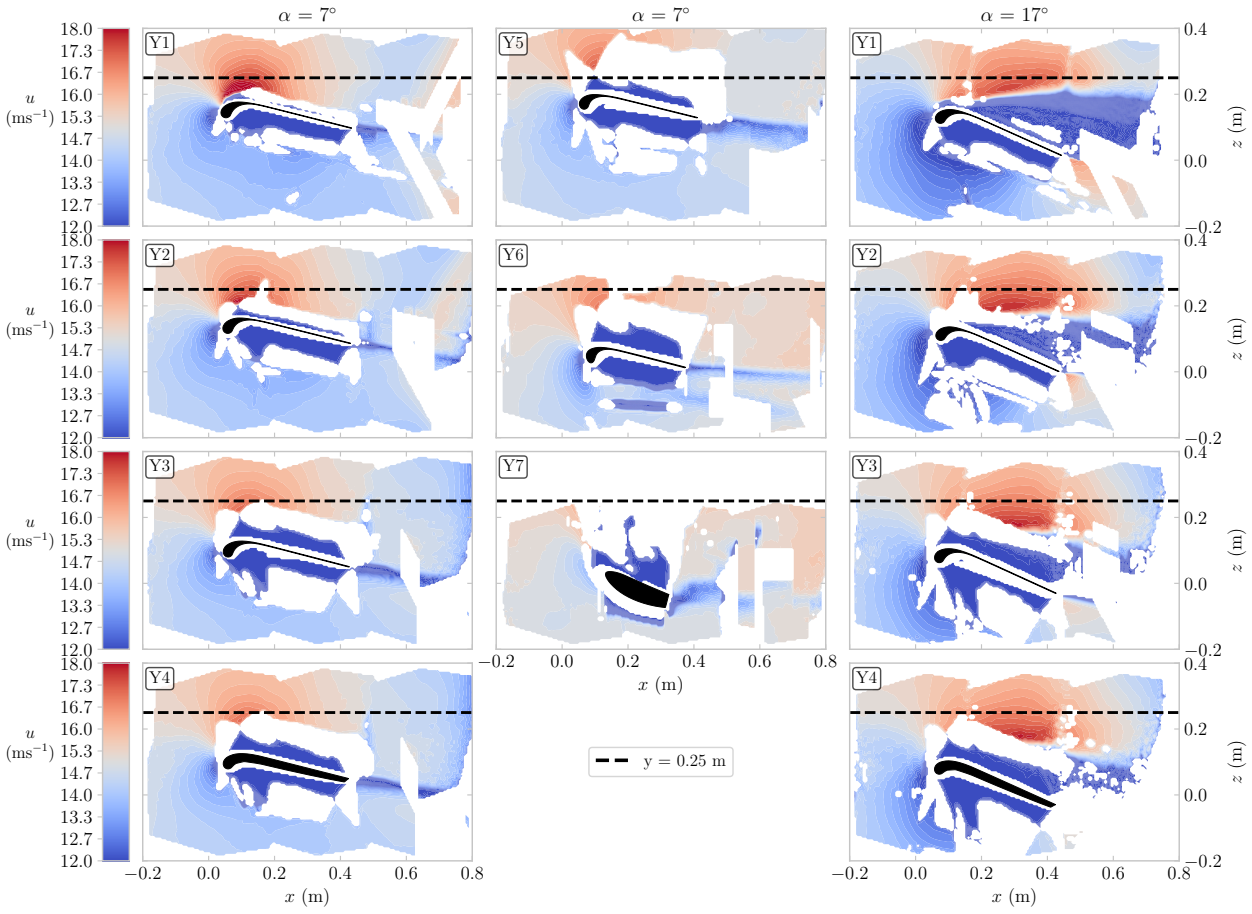

Figure D1. Stitched PIV velocity fields used to assess consistency across sub-plane overlaps. Fields are shown for multiple measurement planes Y_i at $\alpha \approx 7°$ (columns 1–2) and $\alpha \approx 17°$ (column 3). Colours indicate the velocity magnitude u, with the airfoil outline overlaid. The dashed black line at $z = 0.25$ m indicates the threshold above which overlap data are sampled for Table D1.

For each measurement plane Y_i, the streamwise overlap regions between sub-planes were considered when present, and each overlap was analysed independently. Prior to comparison, the velocity fields from the two contributing sub-planes were subjected to identical validity filtering, as described in the manuscript. Within each overlap region, the difference between the two sub-plane velocity fields was computed component-wise over grid points where both fields remained valid. For each

velocity component, the root-mean-square (RMS) of the difference field was then calculated as

$$\mathrm{RMS} = \sqrt{\left\langle (u_A - u_B)^2 \right\rangle}, \tag{D1}$$

where $\langle \cdot \rangle$ denotes averaging over all valid overlap points.

This metric does not represent a full measurement uncertainty. Instead, it provides a local measure of consistency between independently acquired sub-planes at identical spatial locations, and therefore serves as an indicator of the magnitude of residual differences across stitched regions. The resulting RMS differences for all available measurement planes and angles of attack are summarised in Table D1.

Table D1. Stitching uncertainty quantified as the root-mean-square (RMS) difference in the overlap regions, reported for the stitched velocity components u, v, and w. Values are aggregated per measurement plane.

	$\alpha = 7°$							$\alpha = 17°$			
	$Y1$	$Y2$	$Y3$	$Y4$	$Y5$	$Y6$	$Y7$	$Y1$	$Y2$	$Y3$	$Y4$
$\mathrm{RMS}(u_x)$ (ms^{-1})	0.2797	0.3200	0.3197	0.2980	0.6500	0.3370	n/a	0.5974	2.0367	2.6353	2.3660
$\mathrm{RMS}(u_y)$ (ms^{-1})	0.3217	0.6272	0.4960	0.4798	1.0260	0.6659	n/a	0.6599	0.4218	0.6139	0.8322
$\mathrm{RMS}(u_z)$ (ms^{-1})	0.3261	0.6552	0.6033	0.5886	1.2824	0.8904	n/a	0.8203	0.4753	0.4882	0.5179

Overall, the overlap-based RMS differences reported in Table D1 indicate that residual discontinuities between adjacent PIV sub-planes are generally limited to $\mathcal{O}(10^{-1})$–$\mathcal{O}(1)$ ms^{-1} for most measurement planes and angles of attack, with larger values occurring primarily in regions where reconstruction quality is already degraded. These differences quantify the local consistency between independently acquired measurements at identical spatial locations and therefore provide a direct, location-specific indication of stitching-related variability.

At $\alpha = 7°$, RMS differences remain moderate across all planes except $Y5$, where values approach 0.7–1.3 ms^{-1}, where an increased amount of missing data shows in the evaluated region (Fig. D1). For plane $Y7$, insufficient valid data remained above $z = 0.25$ m to compute overlap-based RMS values, reinforcing the decision to exclude this plane from the quantitative analysis in Sect. 3.

At $\alpha = 17°$, RMS differences in planes $Y2$, $Y3$ and $Y4$ exceed 2 ms^{-1} for the streamwise component, corresponding to approximately 13–18% of the free-stream velocity. These elevated values reflect the combined effects of separated flow unsteadiness, increased reflection-induced masking, and reduced correlation quality under stalled conditions. Combined with the Type-A uncertainties reported in Table 5, these observations provided further justification for limiting the quantitative analysis at $\alpha = 17°$ to plane $Y1$ only, as stated in Sect. 3.

For comparison, the Type-A velocity uncertainties reported in Table 5 range from 0.07–0.10 ms^{-1} at $\alpha = 7°$ and 0.18–0.26 ms^{-1} at $\alpha = 17°$. The stitching-related RMS differences are 3–10 times larger than the statistical uncertainty of the mean, indicating that stitching introduces a non-negligible systematic contribution to the total measurement uncertainty, particularly in overlap regions. The analysis is necessarily restricted to a subset of overlap points and does not constitute a comprehensive PIV

uncertainty assessment. Instead, it demonstrates that visible transitions between sub-planes, such as those observable in plane $Y1$ at $\alpha = 17°$ in Fig. D1, correspond to finite and quantified velocity offsets rather than uncontrolled artefacts.

Consequently, the stitched velocity fields are considered sufficiently consistent for the flow analyses presented in Sect. 3, provided that the reported stitching uncertainty is taken into account when interpreting derived quantities.

Appendix E: Defining boundary curves

To obtain aerodynamic properties of a flow field, the methods described in Sect. 2.7 are used and require a boundary curve. Two curve shapes were used, an ellipse and a rectangle, illustrated for both CFD and PIV at $Y2$ and $Y5$ with ~~α is 7~~$\alpha = 7°$ in Fig. E1. The boundary curves are described by a number of nodes N_b. For each boundary node $N_{\mathrm{b,i}}$, the flow field data inside a square of 0.05 m by 0.05 m ~~centered~~ centred at $N_{\mathrm{b,i}}$ was interpolated to populate $N_{\mathrm{b,i}}$.

When ~~analyzing the PIV-measurement~~ analysing the PIV measurement planes, certain boundary curves cross regions without flow field data. Each encountered empty flow field node inside an interpolation square is populated by an additional interpolation using the ~~neighboring~~ neighbouring nodes. Examples of interpolation squares crossing initially empty flow fields are indicated by the black squares in the second column of Fig. E1.

The boundary curves are defined by an x ~~center~~ centre coordinate x_b, a z ~~center~~ centre coordinate z_b, rotation angle, width W_b, height H_b, and N_b. The ~~center~~ centre locations are set equal to the airfoil centroids. To determine suitable W_b and H_b values, a convergence study was done on the lift calculated with Noca's method $C_{\mathrm{l,\,Noca}}$ and the circulation Γ.

The sensitivity results are shown for $Y2$ with ~~$\alpha = 6$~~$\alpha = 7°$ in Fig E2. The first column shows the variation when only changing N_b, where both CFD and PIV results show a converging trend for $C_{\mathrm{l,\,Noca}}$ and Γ. For PIV, the rectangle shape predicts different values. In the second and third columns, the boundary width ~~W_b and height H_b are plotted, and the individual data points are plotted with a color to indicate the % of interpolateddata points; where data points that required more than 1% of interpolation are filtered out~~W_b and height H_b are shown. Each marker is coloured by the percentage of grid points inside the interpolation squares whose u value was missing and therefore locally interpolated, normalised by the total number of grid points inside these squares. Cases exceeding 1 % are excluded from the dataset. The CFD results exhibit good convergence for both variations in W_b and H_b. Both the ellipse and rectangle shapes show close agreement in the values of $C_{\mathrm{l,\,Noca}}$, with only a small deviation in the circulation, Γ. In contrast, the PIV results often fail to converge, with frequent misalignment between the ellipse and rectangle shape predictions.

The 'optimal' number of nodes was determined considering the convergence of circulation Γ and the drag predicted by the Noca's method $C_{\mathrm{d,\,Noca}}$. All planes converged when increasing N_b. A value of 360 nodes was selected for all planes. Determining the parameters W_b and H_b was done iteratively for each plane and α separately. The resulting curves were checked visually and numerically using the % of interpolated empty flow field points to ensure that the curve crossed as ~~much~~ many as possible through the measured flow field. On top of that, the ~~neighboring~~ neighbouring points, e.g., not only 0.4m wide but also 0.41m wide, were checked using the same criteria. A vertical line is present in all plots, indicating the selected values, which, together with the ~~centers~~centres, are reported in Table 6 for all planes.

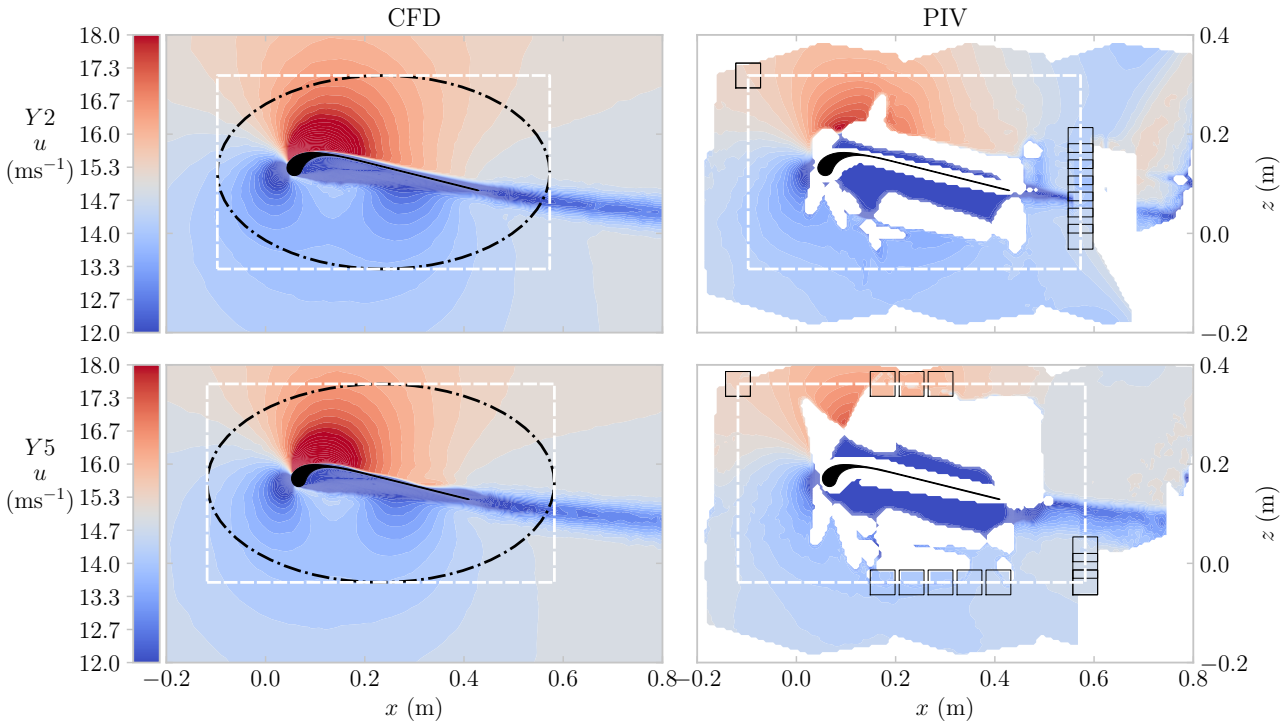

Figure E1. The left column shows CFD and the right column PIV, both colored by the velocity magnitude u. The top row contains the $Y2$ plane and the bottom the $Y5$ plane, both measured at $\alpha = 7^\circ$. The white rectangle and the black ellipse represent the two investigated boundary shapes, and the smaller black squares in the right column represent the PIV locations for which additional interpolation was required to ensure sufficient data presence for populating the boundary nodes.

As the sensitivity analysis showed that the PIV flow field is sensitive to the boundary curve parameters, i.e., does not converge well, the analysis was done on a total of 100 combinations of W_b and H_b and averaged ~~,~~to reduce inconsistencies. The 100 combinations comprise of 10 W_b values and 10 H_b values and span a $\pm$ 10% region, indicated in the plots by the vertical grey band, around the 'optimal' value. A sensitivity analysis was performed on the rotation angle and over a sweep of $\pm 10^\circ$, less than 0.01 difference in $C_{\mathrm{l,\,Noca}}$ and Γ was seen, hence not reported here.

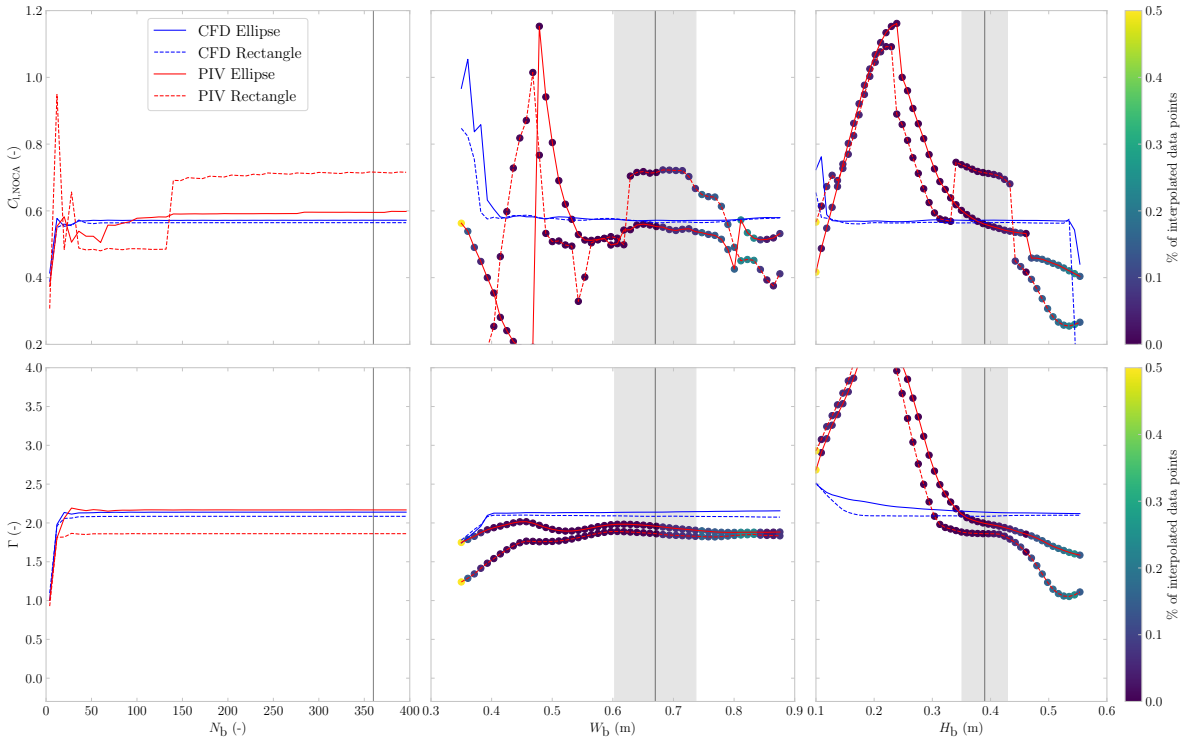

Figure E2. Convergence analysis for $Y2$ the boundary curve setting, i.e. N_b, W_b and H_b, used for calculation $C_{\mathrm{l,\,Noca}}$ presented in the top row and Γ reported in the bottom row. Each plot contains a vertical line, indicating the determined 'optimal' value, and the vertical grey band indicates the region that was used for averaging.

Appendix F: ~~Convergence over the 250 image samples~~

~~To test if the 250 images were sufficient to average the data, the mid-chord suction side measurement of $Y4$ at $\alpha = 17$was analyzed.This plane was chosen as it has the largest uncertainty, see Table 5, rendering it less likely to show good convergence, enabling a conservative estimate.To analyze the convergence, the u_x, u_y and u_z velocities of a specific point are plotted in Fig. A1.To do so, the 250 analyzed images were randomly shuffled; hence, one can not infer anything from the local value pattern.In the local coordinates of the image the point is located at $x = -0.75\mathrm{mm}$ and $z = -118.18\mathrm{mm}$, which corresponds to roughly 0.25 m inboth x and z in the reference frame used in this paper, e.g. as shown in Fig. 6.This analysis confirms that even at this challenging location, the PIV-processed velocity field averaged over 250 images is well-converged. Randomly shuffled u_x, u_y, and u_z velocities of a point above the surface of the airfoil of plane $Y4$ at $\alpha = 17°$.~~

References

Anderson, J. D.: Fundamentals of aerodynamics, McGraw-Hill Inc., 5th edn., ISBN 9780073398105, 2016.

Barlow, J. B., Rae, W. H., and Pope, A.: Low-Speed Wind Tunnel Testing, John Wiley & Sons, New York, 3rd edn., ISBN 978-0471557746, 1999.

Belloc, H.: Wind Tunnel Investigation of a Rigid Paraglider Reference Wing, Journal of Aircraft, 52, 703–708, https://doi.org/10.2514/1.C032513, 2015.

Bensason, D., Sciacchitano, A., and Ferreira, C.: On the wake re-energization of the X-Rotor vertical-axis wind turbine via the vortex-generator strategy, Wind Energy Science Discussions, 2025, 1–37, https://doi.org/10.5194/wes-2025-3, 2025.

Breukels, J.: An Engineering Methodology for Kite Design, Ph.D. thesis, Delft University of Technology, Delft, http://resolver.tudelft.nl/uuid:cdece38a-1f13-47cc-b277-ed64fdda7cdf, 2011.

Cayon, O., Gaunaa, M., and Schmehl, R.: Fast Aero-Structural Model of a Leading-Edge Inflatable Kite, Energies, 16, 3061, https://doi.org/10.3390/en16073061, 2023.

Cayon, O., Watson, S., and Schmehl, R.: Kite as a Sensor: Wind and State Estimation in Tethered Flying Systems, Wind Energy Science Discussions, https://doi.org/10.5194/wes-2024-182, 2025.

Damiani, R., Wendt, F., Jonkman, J., and Sicard, J.: A Vortex Step Method for Nonlinear Airfoil Polar Data as Implemented in KiteAeroDyn, in: Proceedings of the AIAA Scitech 2019 Forum, San Diego, CA, USA, https://doi.org/10.2514/6.2019-0804, 2019.

De Wachter, A.: Deformation and Aerodynamic Performance of a Ram-Air Wing, Master's thesis, Delft University of Technology, https://resolver.tudelft.nl/uuid:786e3395-4590-4755-829f-51283a8df3d2, 2008.

Desai, S., Schetz, J. A., Kapania, R. K., and Gupta, R.: Wind Tunnel Testing of Tethered Inflatable Wings, Journal of Aircraft, 0, 1–18, https://doi.org/10.2514/1.C037437, 2024.

Elfert, C., Göhlich, D., and Schmehl, R.: Measurement of the turning behaviour of tethered membrane wings using automated flight manoeuvres, Wind Energy Science, 9, 2261–2282, https://doi.org/10.5194/wes-9-2261-2024, 2024.

Folkersma, M., Schmehl, R., and Viré, A.: Flow transition modeling on two-dimensional circular leading edge airfoils, Wind Energy, 22, 908–921, https://doi.org/10.1002/we.2329, 2019.

Fritz, E., Boorsma, K., and Ferreira, C.: Experimental analysis of a horizontal-axis wind turbine with swept blades using PIV data, Wind Energy Science, 9, 1617–1629, https://doi.org/10.5194/wes-9-1617-2024, 2024a.

Fritz, E., Ribeiro, A., Boorsma, K., and Ferreira, C.: Aerodynamic characterisation of a thrust-scaled IEA 15 MW wind turbine model: experimental insights using PIV data, Wind Energy Science, 9, 1173–1187, https://doi.org/10.5194/wes-9-1173-2024, 2024b.

Gaunaa, M. et al.: A Computationally Efficient Method for Determining the Aerodynamic Performance of Kites for Wind Energy Applications, in: EWEA Annual Event 2011, European Wind Energy Association (EWEA), https://backend.orbit.dtu.dk/ws/portalfiles/portal/6241674/Gaunaa_poster_EWEA2011presentation%5B1%5D.pdf, 2011.

Huang, M., Sciacchitano, A., and Ferreira, C.: On the wake deflection of vertical axis wind turbines by pitched blades, Wind Energy, 26, 365–387, https://doi.org/10.1002/we.2803, 2023.

Hummel, J., Göhlich, D., and Schmehl, R.: Automatic measurement and characterization of the dynamic properties of tethered membrane wings, Wind Energy Science, 4, 41–55, https://doi.org/10.5194/wes-4-41-2019, 2019.

Jeong, J. and Hussain, F.: On the identification of a vortex, Journal of Fluid Mechanics, 285, 69–94, https://doi.org/10.1017/S0022112095000462, 1995.

LaVision GmbH: LaVision Imaging Solutions for Flow, Spray, Combustion, and Materials Testing, https://www.lavision.de/en/, 2025.

Lebesque, G.: Steady-State RANS Simulation of a Leading Edge Inflatable Wing with Chordwise Struts, Master's thesis, Delft University of Technology, https://resolver.tudelft.nl/uuid:f0bc8a1e-088d-49c5-9b77-ebf9e31cf58b, 2020.

LeBlanc, B. and Ferreira, C.: Estimation of blade loads for a variable pitch vertical axis wind turbine from particle image velocimetry, Wind Energy, 25, 313–332, https://doi.org/10.1002/we.2674, 2022.

Leloup, R., Roncin, K., Bles, G., Leroux, J. B., Jochum, C., and Parlier, Y.: Estimation of the lift-to-drag ratio using the lifting line method: Application to a leading edge inflatable kite, in: Airborne Wind Energy, edited by Ahrens, U., Schmehl, R., and Diehl, M., chap. 19, pp. 339–355, Springer, https://doi.org/10.1007/978-3-642-39965-7_19, 2013.

Lignarolo, L., Ragni, D., Krishnaswami, C., Chen, Q., Ferreira, C. S., and van Bussel, G.: Experimental Analysis of the Wake of a Horizontal-Axis Wind-Turbine Model, Renewable Energy, 70, 31–46, https://doi.org/10.1016/j.renene.2014.01.020, 2014.

Liu, L. Q., Zhu, J. Y., and Wu, J. Z.: Lift and drag in two-dimensional steady viscous and compressible flow, Journal of Fluid Mechanics, 784, 304–341, https://doi.org/10.1017/jfm.2015.584, 2015.

Masure, K. R. G.: Regression Model of Leading Edge Inflatable Kite Profile Aerodynamics, Master's thesis, Delft University of Technology, https://resolver.tudelft.nl/uuid:865d59fc-ccff-462e-9bac-e81725f1c0c9, 2025.

Noca, F., Shiels, D., and Jeon, D.: A comparison of methods for evaluating time-dependant fluid dynamic forces on bodies, using only velocity fields and their derivatives, Journal of Fluids and Structures, 13, 551–578, https://doi.org/10.1006/jfls.1999.0219, 1999.

Oehler, J. and Schmehl, R.: Aerodynamic characterization of a soft kite by in situ flow measurement, Wind Energy Science, 4, 1–21, https://doi.org/10.5194/wes-4-1-2019, 2019.

Poland, J. A. W., Masure, K. R. G., Cayon, O., and Schmehl, R.: [in preparation] Computational aerodynamics for soft-wing design, Wind Energy Science, 2025a.

Poland, J. A. W., van Spronsen, J. M., Gaunaa, M., and Schmehl, R.: Wind Tunnel Load Measurements of a Leading-Edge Inflatable Kite Rigid Scale Model, Wind Energy Science Discussions, https://doi.org/10.5194/wes-2025-77, [preprint], 2025b.

Prasad, A. K.: Stereoscopic particle image velocimetry, Experiments in Fluids, 29, 103–116, https://doi.org/10.1007/s003480000143, 2000.

Prasad, Ajay K. and Adrian, Ronald J.: Stereoscopic particle image velocimetry applied to liquid flows, Experiments in Fluids, 15, 49–60, https://doi.org/10.1007/BF00195595, 1993.

Raffel, M., Willert, C. E., Scarano, F., Kähler, C. J., Wereley, S. T., and Kompenhans, J.: Particle Image Velocimetry: A Practical Guide, Springer, Berlin, Germany, https://doi.org/10.1007/978-3-319-68852-7, 2018.

Sciacchitano, A. and Wieneke, B.: PIV uncertainty propagation, Measurement Science and Technology, 27, 084 006, https://doi.org/10.1088/0957-0233/27/8/084006, 2016.

Viré, A., Demkowicz, P., Folkersma, M., Roullier, A., and Schmehl, R.: Reynolds-averaged Navier-Stokes simulations of the flow past a leading edge inflatable wing for airborne wind energy applications, Journal of Physics: Conference Series, 1618, 032 007, https://doi.org/10.1088/1742-6596/1618/3/032007, 2020.

Viré, A., Lebesque, G., Folkersma, M., and Schmehl, R.: Effect of Chordwise Struts and Misaligned Flow on the Aerodynamic Performance of a Leading-Edge Inflatable Wing, Energies, 15, 1450, https://doi.org/10.3390/en15041450, 2022.

Watchorn, P.: Aerodynamic Load Modelling for Leading Edge Inflatable Kites, Master's thesis, Delft University of Technology, https://resolver.tudelft.nl/uuid:42f611a2-ef79-4540-a43c-0ea827700388, 2023.